Dynamic chromosomal interactions and control of heterochromatin positioning by Ki67

Tom van Schaik[1], Stefano G. Manzo[1], Athanasios E. Vouzas[2,3], David M. Gilbert[2,3] and Bas van Steensel[1,4]

[1]Division of Gene Regulation and Oncode Institute, Netherlands Cancer Institute, Plesmanlaan 121, 1066 CX Amsterdam, the Netherlands

[2]Department of Biological Science, The Florida State University, Tallahassee, 32304, FL, USA

[3]San Diego Biomedical Research Institute, 3525 John Hopkins Court, San Diego, 92121, CA, USA

[4]Correspondence to: b.v.steensel@nki.nl

Abstract

Ki67 forms a protective layer around mitotic chromosomes and is involved in genome positioning around nucleoli during interphase. However, a lack of genomic interaction maps has hampered a detailed understanding of the role of Ki67 in chromatin organization. We used pA-DamID to map genome-Ki67 interactions in three human cell lines and throughout the cell cycle. In mitosis, Ki67 shows a surprising preference for the distal 15-30 Mb of each chromosome. Early in interphase, when Ki67 is present in pre-nucleolar bodies, this is replaced by a pattern of large domains that overlaps with late-replicating DNA, which gradually shifts towards small chromosomes. Nucleolar perturbations indicate that these cell cycle dynamics correspond to nucleolar maturation during interphase. Furthermore, Ki67 competes with the nuclear lamina for interaction with late-replicating DNA, and controls replication timing at (peri)centromeric regions. Together, these results reveal a highly dynamic choreography of genome interactions and roles for Ki67 in genome organization.

INTRODUCTION

Ki67 is a chromosomal, nuclear and nucleolar protein that is widely used as a marker for cellular proliferation [reviewed in 1, 2, 3]. It has been implicated in chromatin biology in various stages of the cell cycle. During mitosis, Ki67 is a key component of the peri-chromosomal layer (PCL) [4, 5], where it acts as surfactant to prevent chromosomal intermingling [6, 7]. Following anaphase, Ki67 changes from a repelling into an attracting behavior to exclude cytoplasmic proteins and compact chromosomes [8]. Early in interphase Ki67 accumulates in pre-nucleolar bodies (PNBs), which are punctate structures containing rRNA precursors and various proteins [9]. These PNBs gradually fade away as several mature nucleoli are formed [10-12]. In these mature nucleoli Ki67 is positioned specifically at the nucleolar rim.

Together with the nuclear lamina (NL), the nucleolus is a major hub for heterochromatin, as illustrated by both microscopy [13, 14] and genomics observations [15-18]. Often, individual heterochromatic genomic loci are stochastically distributed between the NL and nucleoli, with variable preference for one or the other [18-20]. Additionally, disruption of one of the two structures may enhance interactions with the other [20, 21], which may indicate a competitive mechanism. Interestingly, depletion of Ki67 has been shown to lead to a loss of heterochromatin around the nucleolus [22], suggesting that it may tether heterochromatin to the nucleolus.

So far, most studies of the interplay between Ki67 and chromatin have relied on microscopy observations [e.g., 5, 22, 23]. While these experiments have been highly informative, it has remained unclear how exactly Ki67 interacts with the genome throughout the cell cycle. Genome-wide interaction data would greatly enhance this understanding, and permit comparisons with other nuclear positioning data, the epigenetic landscape and functional readouts of the genome such as transcription and replication timing.

Here, we provide such data using our recently developed pA-DamID technology, which allows for visualization of protein-DNA interactions in situ and generation of genome-wide interaction maps with high temporal resolution [24]. Our results uncover remarkably dynamic interactions of Ki67 with the genome of human cells, and provide insights into its roles in heterochromatin organization and replication timing.

RESULTS

pA-DamID captures genome – Ki67 interactions

We used our recently developed pA-DamID method to profile Ki67 interactions with the genome. pA-DamID allows us to both create maps of genome-wide protein-DNA interactions with high temporal resolution, and to visualize these interactions in situ with the ^{m6}A-Tracer protein (**Fig 1A**) [19, 24]. Following pA-DamID with a Ki67 antibody in hTERT-RPE, HCT116 and K562 human cell lines, we indeed observe that ^{m6}A-Tracer binding (and hence the interaction of Ki67 with the genome) is enriched at nucleoli stained by Ki67, compared to a free Dam control (**Fig 1B, C**). ^{m6}A-Tracer binding occurs mostly at the edges of nucleoli, indicating that Ki67 preferentially contacts DNA at the nucleolar periphery. However, Ki67 is not exclusively localized at nucleoli and may be locally enriched elsewhere, such as the nuclear periphery (**Fig 1B**, orange arrow). This overlaps with ^{m6}A-Tracer staining, indicating that Ki67 at these sites can also engage in genome interactions. In addition, a moderate homogeneous ^{m6}A-Tracer signal throughout the nucleus may be caused by low concentrations of DNA-interacting Ki67 in the nuclear interior, but also from non-specific antibody binding.

We then processed these ^{m6}A-tagged DNA samples for high-throughput sequencing to identify the genomic regions that interact with Ki67. We first describe results in unsynchronized cells; below we discuss the dynamics throughout the cell cycle. As described previously [24], pA-DamID utilizes a free Dam control to normalize for DNA accessibility and amplification biases [25]. After this Dam normalization we observed a striking domain-like pattern of Ki67 binding to the genome (**Fig S1A**). We balanced data resolution and reproducibility by using 50kb averaging bins that yield acceptable Pearson correlation coefficients between independent replicate experiments in the range of 0.40 - 0.80 (**Fig S1B, C**); at smaller bin sizes the data were too noisy to be informative.

To validate these interaction maps, we used an HCT116 cell line with mClover- and AID-tagged Ki67, which allow for protein visualization and rapid protein depletion upon addition of auxin, respectively [7]. Incubation of these cells with auxin for 24 hours resulted in a near-complete depletion of mClover fluorescence, but only a partial decrease in Ki67 immunostaining signal (**Fig S1D, E**). This difference may be caused by the higher sensitivity of indirect immunofluorescence [7]. Genome-wide mapping of Ki67 interactions with pA-DamID resulted in a strong signal loss at the Ki67 interaction domains upon addition of auxin (**Fig S1F, G**). We assume that the remaining signals (e.g., on chr22) result from some residual Ki67 protein. These data verify that Ki67 interaction domains are specific for Ki67 and not caused by technical artifacts.

Finally, as Ki67 is a very large protein (~350 kDa), we reasoned that the location of the antibody epitope could affect the observed interaction patterns. Ki67 contains protein binding domains and a DNA binding domain, positioned at the N and C-terminus, respectively [reviewed in 2]. The initial antibody used was generated against a peptide sequence roughly in the middle of the protein (~1150/3256 amino acids), so we chose two additional antibodies to target each protein end. As before, immunostaining following auxin-

mediated Ki67 depletion confirms antibody specificity to Ki67 (**Fig S2A**). Following pA-DamID, only the C-terminus antibody results in ^{m6}A-Tracer enrichment around Ki67 domains (**Fig S2B**) and yields a genome-wide domain pattern that is similar to that of the initially used antibody (**Fig S2C**). With the N-terminus antibody some of this domain pattern can also be observed, but the data quality is rather poor (**Fig S2D, E**), possibly because the antibody epitope is too far from the DNA. These results thus show that Ki67 profiles can be reproduced with different antibodies, and are in accordance with C-terminal location of the DNA binding domain.

Combined, we conclude that application of pA-DamID results in robust genome-wide Ki67 interaction maps, although the data resolution remains limited to about 50 kb. The ^{m6}A-Tracer staining indicates that interactions of Ki67 with the genome are enriched near nucleoli, but may also occur elsewhere.

Ki67 binding varies between cell types, but is consistently enriched at small chromosomes and near centromeres

Differences in Ki67 interactions among cell types are most apparent on large chromosomes (**Fig 1D, S3A**). In contrast, interactions are more consistent on small chromosomes (**Fig S3A**), and more frequent as illustrated by a higher dynamic range compared to larger chromosomes (**Fig 1E**). Small chromosomes are typically positioned in the nuclear interior and in the vicinity of nucleoli [26, 27], suggesting that these interactions involve nucleolar Ki67.

Nucleoli are formed around rDNA repeats that are positioned on the p-arm of several human chromosomes, next to the centromere. We therefore expected to find Ki67 binding near these regions. Indeed, rDNA-containing chromosomes often have the highest Ki67 interaction scores, even though sections of these chromosomes are depleted for Ki67 (indicated by negative values in the boxplots) (**Fig 1E**). However, Ki67 may lack affinity for rDNA sequences themselves as these show no enrichment in our data (**Fig S3B**). Ki67 interactions are enriched up to several Mb outside centromeres for all cell types (**Fig 1F**). While this scales with chromosome size and partially with rDNA presence, sequences near centromeres are enriched for Ki67 interactions on all chromosomes (**Fig 1G**).

Cell cycle dynamics of Ki67 interactions

The interpretation of the Ki67 interaction profiles could be confounded by the variable location of Ki67 during the cell cycle. Microscopy studies have shown that Ki67 coats chromosomes during mitosis, localizes to pre-nucleolar bodies (PNBs) in early G1 and slowly transfers to nucleoli during interphase [4, reviewed in 28]. We hypothesized that these transitions would be accompanied by a shift in genomic interactions. To test this, we synchronized RPE cells in metaphase and harvested cells at several time points during the cell cycle to profile Ki67 interactions [24].

We first prepared cells for ^{m6}A-Tracer microscopy to validate the localization of Ki67 and its DNA interactions. Cells synchronized in metaphase show clearly condensed chromosomes with Ki67 and ^{m6}A-Tracer signals at the periphery of the chromosomes (**Fig**

117 2A), although individual chromosomes are difficult to distinguish after pA-DamID,
118 presumably due to several hours of nuclear permeabilization without fixation (c.f. Fig 2A and
119 3A). One hour after synchronization, when cells have entered interphase, Ki67 is spread
120 throughout the nucleus in numerous PNBs (Fig 2A). Later time points show a gradual
121 repositioning of Ki67 from small PNBs to several mature nucleoli. At all interphase time
122 points ^{m6}A-Tracer signal is enriched near Ki67 (Fig 2A, B), which indicates that a
123 redistribution of Ki67 also affects its DNA interactions.
124 We then processed these samples for genome-wide mapping of the ^{m6}A-tagged Ki67
125 interaction sites. For subsequent quantitative analyses of Ki67 interactions, we first
126 converted the $\log_2$-ratios to z-scores. This equalizes any variable dynamic ranges between
127 conditions and replicates without affecting the data distribution, similar to previous work for
128 Lamin B1 interactions during the cell cycle [24]. The genome-wide mapping data reveal
129 several interesting patterns (Fig 2C). First, during mitosis (t = 0 h) Ki67 interactions are
130 enriched at the distal ends of the chromosome ends (Fig 2C, D). The enrichment extends up
131 to 15-30 Mb from the telomere and scales with chromosome size. Second, early in G1 phase
132 (t = 1 h), Ki67 interactions are more evenly distributed among all chromosomes compared to
133 unsynchronized cells, with increased and decreased interactions for large and small
134 chromosomes, respectively (Fig 2E). Third, during interphase, Ki67 interactions are
135 gradually lost on large chromosomes in favor of smaller chromosomes (Fig 2C, F).
136 Remarkably, chromosome X does not follow these trends. This may be caused by active
137 repositioning of the inactive chromosome X to nucleoli during S-phase [29, 30]. Because
138 mitosis is relatively quick and nucleoli mature in a few hours, Ki67 profiles from
139 unsynchronized cells are probably strongly enriched for interactions with mature nucleoli.
140 These changes in genome-wide binding patterns roughly coincide with the sequential
141 repositioning of Ki67 from the chromosomal periphery to PNBs, and then to mature nucleoli.
142 To further investigate the link between Ki67 dynamics during interphase and the nucleolar
143 maturation from PNBs, we disrupted nucleoli in hTERT-RPE cells with a short osmotic
144 shock. Upon recovery, the process of PNB formation and nucleolar maturation is repeated
145 [31]. Indeed, we find that Ki67-containing PNBs are strongly enriched after 30 minutes of
146 recovery and mostly lost again after 180 minutes (Fig S4A). pA-DamID maps from these
147 cells show that the 30-minute time point mostly resembles early G1, while the 180-minute
148 time point is more similar to late G1. Similar to early interphase, this transition corresponds
149 to an increase of Ki67 interactions on small chromosomes (Fig S4B, C). Thus, we conclude
150 that cell cycle dynamics of Ki67 interactions correspond to nucleolar maturation during
151 interphase.
152
153 **Release of Ki67 from nucleoli drastically changes its DNA interactions**
154 The results presented so far suggest that Ki67 has a binding potential for all chromosomes,
155 but its distribution is dynamically influenced by its cell cycle regulated interactions with PNBs
156 and nucleoli. To test the importance of nucleolar confinement further, we released Ki67 from
157 nucleoli by adding a low dose of actinomycin D (ActD; 50 ng/mL) for 3 hours. ActD at this
158 concentration specifically inhibits PolI transcription and results in nucleolar breakdown [20,

159 32]. As a result, Ki67 is no longer restricted to nucleoli and shows distinct patterns from other
160 nucleolar markers (i.e. MKI67IP) (**Fig 3A, S4D-E**). Ki67 localization to mitotic chromosomes
161 is not affected by ActD (**Fig 3A**, orange arrow).
162 pA-DamID mapping shows that this nucleolar breakdown affects Ki67 binding to the
163 genome, but in different ways depending on the cell type (**Fig 3B**). In hTERT-RPE and
164 HCT116 cells, the genomic preference of Ki67 seems mostly maintained but interactions
165 show strong quantitative differences (**Fig 3B**). This includes an overall shift of Ki67 from
166 small chromosomes to large chromosomes (**Fig 3C**). In contrast, the interaction pattern in
167 K562 cells is more broadly altered (**Fig 3B**), although a reduction of Ki67 interactions with
168 rDNA-containing chromosomes is shared with the other two cell types (**Fig 3C**). All three cell
169 types also exhibit a consistent loss of Ki67 interactions near centromeres, again most clearly
170 for rDNA-containing chromosomes (**Fig 3D**). Combined, these results illustrate that nucleolar
171 integrity is required for a normal Ki67 interaction pattern across the genome, in particular for
172 the preference at small and rDNA-containing chromosomes.
173
174 **Ki67 and Lamin B1 interactions partially overlap and together mark the late-replicating**
175 **genome**
176 There is at least a partial redundancy of heterochromatin positioning between nucleoli and
177 the NL [reviewed in 33, 34]. To determine whether we could also observe this in our data, we
178 compared our pA-DamID maps of Ki67 and Lamin B1 [24]. Overall, both proteins interact
179 with mostly similar genomic domains, although their relative interaction frequencies vary
180 strongly (**Fig 4A**). Often, among the domains bound by both proteins, Ki67 and Lamin B1
181 seem anti-correlated, where domains with the highest Ki67 signals are generally lower in
182 Lamin B1 signals, and vice-versa (**Fig 4A**, orange arrows). This partial anti-correlation is
183 visible as the "head" of a hammer-shaped scatter plot, particularly in hTERT-RPE cells (**Fig**
184 **4B**, top panels).
185 Late replicating DNA is known to be enriched at both the nuclear periphery and
186 nucleolus [reviewed in 35]. Indeed, analysis of published maps of replication timing [36]
187 showed strong overlap of late-replicating domains with both the Ki67 and Lamin B1 domains
188 (**Fig 4A**). Strikingly, the late-replicating regions overlap almost perfectly with the hammer-
189 heads in the Ki67 versus Lamin B1 scatter plots (**Fig 4B**, middle panels). Thus, virtually all
190 late-replicating domains are covered by either of the two proteins, and among these domains
191 competition may lead to a variable balance between the two proteins.
192
193 **Ki67 competes with the nuclear lamina for heterochromatin in HCT116 cells**
194 To test this competition, we used the HCT116 Ki67-AID cell line and mapped Lamin B1
195 interactions following 24 hours of Ki67 depletion. Additionally, given the roles of Ki67 in
196 mitosis and the reorganization of the genome afterwards, we combined Ki67 depletion with
197 two cell synchronization strategies. First, Ki67 was depleted during a double thymidine block.
198 These cells undergo a single cell division and the synchronization prevents any cell cycle
199 perturbation that Ki67 depletion may induce. Second, to specifically test whether mitosis is
200 required for DNA repositioning, Ki67 was depleted in G2-arrested cells using a CDK1

201 inhibitor (**Fig 5A**). Flow cytometry confirmed cell synchronization with and without Ki67
202 depletion (**Fig 5A**, bottom panels). We first verified the Ki67 pA-DamID patterns in
203 synchronized cells with normal Ki67 levels (i.e., not treated with auxin). Here, we found a
204 shift of Ki67 between S-phase and G2 cells that correlates with chromosome size (**Fig 5B**),
205 akin to the progressive shift towards smaller chromosomes that we observed during
206 interphase in hTERT-RPE cells (**Fig 2C, F**).
207 Ki67 depletion induces small quantitative differences in Lamin B1 interactions (**Fig**
208 **5C**, orange arrows). Importantly, increases in Lamin B1 interactions are most prominent in
209 regions that were originally bound by Ki67 (**Fig 5D**). This effect is most apparent in S-phase
210 cells (which had progressed through mitosis), but is still present in cells blocked in G2 (with
211 Pearson correlations between the initial Ki67 score and Lamin B1 difference of
212 approximately 0.3 and 0.2 for the two conditions, respectively). Passage through mitosis is
213 thus not required to change genome positioning. We conclude that Ki67 counteracts Lamin
214 B1 interactions of a subset of late-replicating domains.
215
216 **Ki67 promotes timely replication of centromeres**
217 Next, we asked whether Ki67 depletion affected the replication timing of the regions that it
218 interacts with. We tested this by Repli-seq [37], 24 hours after Ki67 depletion in
219 (unsynchronized) HCT116 cells (**Fig 5E, F**). While replication timing across most of the
220 genome remained unaffected by this depletion, we did observe a small but consistent delay
221 in replication timing in peri-centromeric regions (**Fig 5G, H**). Centromeric sequences, which
222 cannot be uniquely mapped to individual chromosomes, also showed a delayed replication
223 timing upon Ki67 depletion (**Fig S5A**). The replication timing observations are different from
224 Lamin B1 interactions that increased near centromeres but also on other domains with high
225 Ki67 scores (**Fig 5E,** purple arrows, **S5B, C**). Thus, Ki67 specifically regulates the replication
226 timing of (peri-)centromeric regions.
227
228 **No evidence for direct gene repression by Ki67**
229 Genes in late replicating and NL-associated domains generally show little transcriptional
230 activity [15, reviewed in 35, 38-40]. Indeed, mRNA-seq data show that genes in the above-
231 mentioned scatterplot hammer-head predominantly are lowly transcribed (**Fig S5D**). In line
232 with this, genes with high levels of Ki67 tend to be inactive, particularly in hTERT-RPE and
233 HTC116 cells.
234 We then asked whether Ki67 contributes directly to the transcriptional repression of
235 these genes. Several studies have found changes in gene activity upon Ki67 loss [22, 30,
236 41, 42], but none could attribute this to direct effects, in part because the binding pattern of
237 Ki67 was not known. We therefore generated RNA-seq data in the HCT116 Ki67-AID cells.
238 We synchronized these cells in S-phase, to rule out any cell cycle effects that Ki67 depletion
239 may have in these cells (**Fig 5A**). Intriguingly, we find that gene expression is largely
240 unaffected by acute Ki67 depletion, with only three genes reaching our significance cut-off:
241 ALDH1A3, CYP1A1 and HAS3 (**Fig S5E**). We cannot link these genes to initial Ki67 binding

242 or Ki67 biology. A similar result was obtained in a recent study that also employed auxin-
243 mediated Ki67-AID depletion in HCT116 cells [42].
244 We also compared Ki67 interactions with gene expression data following Ki67
245 depletion in hTERT-RPE cells [30]. Unlike HTC116, these cells express p21, which causes
246 cell cycle perturbations in response to Ki67 loss, and concomitant differential expression of
247 thousands of genes [30]. Our re-analysis of these data indicates that the changes in gene
248 expression do not correlate with initial Ki67 binding (**Fig S5F**). This further indicates that
249 Ki67 binding is not directly involved in gene silencing.
250
251 **Ki67 binding correlates positively with H3K9me3 and negatively with H3K27me3**
252 Finally, we compared the Ki67 patterns to those of the main repressive histone modifications
253 H3K27me3 and H3K9me3 (**Fig 6A**). Remarkably, these marks are strongly correlated with
254 the balance between Ki67 and Lamin B1. In hTERT-RPE and HCT116 cells the scatterplot
255 hammer-head shows a strong partitioning, with Ki67 interactions being positively linked to
256 H3K9me3 but not H3K27me3 (**Fig 6B**). In K562 cells the preference of H3K9me3 for Ki67-
257 rich regions is less pronounced.
258 Following acute Ki67 depletion in HCT116 cells (**Fig 5**), H3K27me3 and H3K9me3
259 are only subtly affected (**Fig 6C**). The effect sizes seem smaller than for Lamin B1
260 interactions. Interestingly, we observed a mild increase in H3K27me3 levels for regions
261 originally bound by Ki67 (**Fig 6D**), suggesting that Ki67 interactions suppress H3K27me3
262 deposition. The effect of Ki67 depletion on H3K9me3 is more complicated. Initial Ki67
263 binding is weakly correlated with an increase in H3K9me3 in G2-synchronized cells, but we
264 do not observe this in cells in S-phase (**Fig 6D**).
265
266
267 **DISCUSSION**
268
269 Microscopy studies have illustrated that Ki67 and nucleoli are important contributors to
270 genome organization, in particular for heterochromatin positioning and the separation of
271 mitotic chromosomes [5-8, 22]. However, a lack of genome-wide interaction profiles of Ki67
272 has hampered a detailed understanding of how this protein shapes and regulates the
273 genome. In this work, we applied pA-DamID to profile genome – Ki67 interactions in several
274 human cell lines and throughout the cell cycle.
275 One of the fascinating aspects of Ki67 is its role on mitotic chromosomes, where it
276 establishes the peri-chromosomal layer [4, 5, 43, 44] and acts as a surfactant that prevents
277 chromosomal intermingling [6, 7]. Surprisingly, our pA-DamID data indicate that Ki67 does
278 not coat mitotic chromosomes homogeneously, but instead shows a preference for the distal
279 ~15-30 Mb of each chromosome arm. We cannot rule out that Ki67 is selectively lost from
280 the proximal regions during the permeabilization step that is part of the pA-DamID protocol.
281 For example, Ki67 shows increased mobility during mitosis [45], and prolonged
282 permeabilization may select for a more stable binding population. Because the interaction
283 frequencies reported by pA-DamID are relative rather than absolute, we emphasize that

284 these results do not imply that the central chromosomal regions are completely devoid of
285 Ki67, only that their occupancy is lower.
286 The enrichment of Ki67 at the distal regions may be caused by encapsulation of the
287 ends of condensed chromosomes, which would result in a local increase of surface area and
288 thus a relative increase in Ki67 signal. An alternative and not mutually exclusive explanation
289 is that the chromosomal ends are typically facing away from the chromosomal territory [46],
290 and thereby recruit more Ki67. This hypothesis is supported by our previous observations
291 that the distal ends of chromosomes (up to ~25 Mb) are enriched for Lamin B1 interactions
292 in early G1 [24], suggesting that these regions are at the periphery of the chromosomal
293 territory upon establishment of the NL. Similarly, LAP2α has been reported to associate with
294 the ends of mitotic chromosomes [47]. Possibly, Ki67 is enriched at mitotic chromosome
295 ends because its surfactant activity is particularly critical to prevent telomere-telomere
296 fusions. In support of this hypothesis, chromosome bridges – which are typical of such
297 fusions – have been detected in mitotic cells that lack Ki67, although DNA damage
298 elsewhere may also cause such bridges [42].
299 Following mitosis, we observed a rapid rearrangement of Ki67-DNA interactions
300 across the genome. Within ~1 hour, Ki67 moves to many late-replicating domains. This
301 transition may be triggered by dephosphorylation of Ki67 [45, 48]. Our data are in
302 accordance with early microscopy observations that Ki67 overlaps with most large
303 heterochromatin domains in early interphase [49]. However, our results also show that Ki67
304 gradually redistributes during early G1 from large to smaller chromosomes. This
305 redistribution roughly coincides with the relocation of Ki67 from PNBs to nucleoli, and is
306 reverted by perturbations that release Ki67 from nucleoli and re-establish PNBs. We
307 therefore propose that Ki67 in PNBs interacts with late-replicating domains throughout the
308 genome, while upon sequestration of Ki67 at nucleoli these interactions become restricted to
309 small chromosomes. In support of this model, small chromosomes tend to be positioned
310 near nucleoli [27, 50].
311 Our results implicate Ki67 as one of the proteins that modulate the distribution of late-
312 replicating DNA between nucleoli and the NL [reviewed in 33, 34, 40]. Most likely this is due
313 to direct interaction of Ki67 with a subset of late-replicating regions. It is interesting to note
314 that both Ki67 and lamins preferentially bind AT-rich DNA in vitro [51, 52], which matches
315 observations that both nucleolus- and lamina-associated domains are AT-rich [16, 53].
316 However, it is likely that other proteins besides Ki67 mediate nucleolar interactions. For
317 example, different from our Ki67 profiles, a subset of nucleolar interactions shows
318 enrichment for H3K27me3 and early-replicating DNA [18]. Moreover, Ki67 is slowly
319 degraded in G1 and completely absent in senescent cells [43, 54, 55], yet these cells largely
320 maintain their nucleolus - genome interactions [17]. Exceptions are alpha-satellite
321 sequences (at centromeres) and H3K9me3-marked chromatin, which lose nucleolar
322 positioning upon senescence [17]. Our data show that these regions strongly interact with
323 Ki67, supporting a direct role in nucleolus tethering.
324 Upon Ki67 depletion, we observed a surprising delay in replication timing specifically
325 at (peri-)centromeres. These regions show increased Lamin B1 interactions, yet other

326 regions that reposition towards the NL are not affected in their replication. Rather, we
327 speculate that Ki67 directly affects replication of centromeres, which are known for their
328 early and tightly regulated DNA replication [reviewed in 56, 57]. The perturbed replication
329 may be consequence of increased transcription of alpha-satellite sequences following Ki67
330 depletion [58]. Resulting transcription-replication conflicts could result in delayed and
331 incomplete DNA replication, as was recently shown following rapid CENP-A depletion [59].
332
333
334 **METHODS**
335
336 ***Experimental methods***
337
338 **Cell culture**
339 hTERT-RPE cells (ATCC CRL-4000), HCT116 cells (ATCC CCL-247) and K562 cells (ATCC
340 CCL-243) were cultured according to their ATCC handling procedure, except that cells were
341 passaged using 0.05% Trypsin-EDTA (Gibco) instead of 0.25%. Adherent cells (hTERT-RPE
342 cells and HCT116 cells) were harvested with 0.05% Trypsin-EDTA, which was inactivated
343 with complete medium.
344 HCT116 Ki67-miniAID-mClover cells (Ki67-AID in short) were kindly provided by M.
345 Takagi and cultured as wildtype HCT116 cells. Ki67 depletion was induced by adding 500
346 μM auxin (from a 1 mM stock solution) (Sigma-Aldrich), or a similar amount of DMSO for
347 control cells.
348 All cells were tested for mycoplasma presence every 2 months.
349
350 **Cell cycle synchronization**
351 Cell cycle synchronization of hTERT-RPE was performed as described previously [24]. Cells
352 were cultured for 24 h in 75 cm^2 flasks to reach ~50% confluency, after which mitotic cells
353 were enriched for using a sequential synchronization strategy of G2 arrest (16 h of 10 μM
354 RO-3306, CDK1 inhibitor) followed by metaphase blocking (1.5 h of 25 ng/mL nocodazole,
355 microtubule inhibitor). Mitotic cells were harvested by shake-off and immediately processed
356 for pA-DamID or replated in complete medium for interphase time points. Light microscopy
357 confirmed successful mitotic synchronization, and adherence and cell division of the replated
358 cells. Replated cells were harvested after 1, 3, 6 and 10 h.
359
360 **Osmotic shock**
361 hTERT-RPE cells were cultured overnight in multiple 10 cm dishes with 10 mm cover slips.
362 Cells were washed in pre-warmed 1x phosphate-buffer saline (PBS), after which nucleoli
363 were disrupted by a 15-minute osmotic shock (0.2x PBS) [31]. Cells were released in
364 complete medium and harvested for pA-DamID after 30 and 180 minutes. To verify nucleolar
365 reassembly, cover slips with attached cells were removed before harvesting, washed in PBS
366 and fixed for 10 minutes in 2% formaldehyde/PBS.
367

368 **Actinomycin D treatment**
369 hTERT-RPE cells, HCT116 cells and K562 cells were cultured overnight in two 10 cm dishes
370 with 10 mm cover slips. PolI transcription was specifically inhibited using a 3 h treatment of
371 50 ng/mL actinomycin D (from a 1 mg/mL stock solution). A similar amount of DMSO was
372 added to control cells. Cover slips were removed and cells were fixed with 2%
373 formaldehyde/PBS to verify nucleolar disruption and Ki67 redistribution. For K562 cells, the
374 cover slips were coated with poly-L-lysine to immobilize the cells. Remaining cells were
375 harvested for pA-DamID experiments.
376
377 **HCT116 Ki67-AID synchronization experiments**
378 HCT116 Ki67-AID (M. Takagi) were synchronized using a sequential arrest into S-phase and
379 G2-phase. First, cells were cultured overnight in 2.5 mM thymidine to block cells in S-phase,
380 and then washed two times in pre-warmed PBS and once in complete medium. For S-phase
381 cells, the cells were released in complete medium for 8 h, after which they were incubated
382 with 2.5 mM thymidine for another 16 h. For G2-phase cells, the cells were released on
383 complete medium supplemented with 10 μM RO-3306 (CDK1 inhibitor) for 24 h. During the
384 last 24 h, Ki67 depletion was induced by adding 500 μM auxin (Sigma-Aldrich), or a similar
385 amount of DMSO for control cells. For all conditions, cells were cultured in 10 cm dishes with
386 10 mm poly-L-lysine coated coverslips. Before harvesting cells for pA-DamID, cover slips
387 were removed, washed in PBS and cells were fixed for 10 minutes with 2%
388 formaldehyde/PBS to verify Ki67 depletion. Additionally, cells synchronization was confirmed
389 using ethanol fixation and DNA staining with 1 μg/mL DAPI [37]. DNA content was measured
390 using flow cytometry on an Attune NxT (Invitrogen, Thermo Fisher Scientific).
391
392 **pA-DamID**
393 pA-DamID experiments were performed as described previously [24]. One million cells were
394 collected by centrifugation in 1.5 mL Eppendorf tubes (3 minutes, 500g, at 4°C), washed in
395 400 μL of ice-cold PBS and subsequently washed in 400 μL of ice-cold digitonin wash buffer
396 (DigWash) (20 mM HEPES-KOH pH 7.5, 150 mM NaCl, 0.5 mM spermidine, 0.02%
397 digitonin, cOmplete Protease Inhibitor Cocktail (Roche # 11873580001)). Cells were
398 resuspended in 200 μL DigWash supplemented with a primary antibody and rotated for 2
399 hours at 4 °C. After a DigWash wash step, cells were resuspended in 200 μL DigWash
400 supplemented with 1:200 pA-Dam protein (~40 units of Dam activity) and rotated for 1 hour
401 at 4 °C. After two wash steps with DigWash, Dam activity was induced by resuspension in
402 100 μL DigWash supplemented with 80 μM S-adenosyl-methionine (SAM) (NEB, B9003S)
403 and incubated at 37 °C for 30 minutes. For every experimental condition, one million cells
404 were also processed without antibodies or pA-Dam protein, but instead incubated with 4
405 units of Dam enzyme (NEB, M0222L) during the activating step. This freely diffusing Dam
406 moiety serves as control to account for DNA accessibility and amplification biases.
407 For the primary antibody incubation, we used 1:100 dilutions for antibodies against
408 Ki67 (Abcam ab15580, rabbit), N-terminal Ki67 (Human Protein Atlas HPA001164-25UL,
409 rabbit), C-terminal Ki67 (Novus NB600-1252-0.1ml, rabbit), H3K27me3 (CST C36B11,

410 rabbit), and H3K9me3 (Diagode C15310193, rabbit). A 1:400 dilution was used for the
411 antibody against Lamin B1 (Abcam ab16048, rabbit).
412 At this point, either genomic DNA was isolated and processed for high-throughput
413 sequencing, or cells were diluted in PBS and plated on poly-L-lysine coated cover slips for
414 30 minutes, followed by 10 minutes fixation with 2% formaldehyde/PBS and immunostaining.
415 These cover slips were first coated with 0.1% (w/v) poly-L-lysine (Sigma-Aldrich, #P8920) for
416 15 minutes, washed with H_2O (once) and PBS (3 times) and stored in 70% ethanol for later
417 use. Samples were prepared for single-end 65 bps Illumina Hi-seq sequencing as described
418 previously [60, 61], except that the DpnII digestion was omitted. Approximately 15 million
419 reads were sequenced for every Ki67 and Dam control sample to ensure high quality Ki67
420 interaction data, and approximately 5 million reads were sequenced for Lamin B1,
421 H3K27me3 and H3K9me3 libraries.
422
423 **Repli-seq**
424 Following 24 h of Ki67 depletion in HCT116 Ki67-AID cells (see above), BrdU was added to
425 a final concentration of 100 μM and cells were incubated at 37 °C for another 2 h. Cells were
426 fixed in ice-cold ethanol and processed for Repli-seq as described [37]. Libraries were
427 sequenced with approximately 10 million 150 bps paired-end reads per sample on an
428 Illumina NovaSeq 6000.
429
430 **RNA-seq**
431 HCT116 Ki67-AID cells were synchronized in S-phase with 24 h of Ki67 depletion (see
432 above). RNA was isolated using the Qiagen RNeasy column purification kit, after which
433 sequencing libraries were prepared using the Illumina TruSeq polyA stranded RNA kit.
434 Libraries were sequenced with approximately 25 million 2x54 bps paired-end reads on an
435 Illumina NovaSeq 6000.
436
437 **Immunostaining and microscopy**
438 Cover slips with formaldehyde fixed cells were washed with PBS, permeabilized with 0.5%
439 NP40/PBS for 20 minutes and blocked with 1% BSA/PBS for 1 h. Cover slips were
440 incubated with primary antibodies at room temperature for 1 h, and washed three times with
441 PBS. Next, cover slips were incubated with secondary antibodies at room temperature for 45
442 minutes. After one wash with PBS, DNA was stained with 1 μg/mL DAPI for 10 minutes,
443 followed by two washes with PBS and one with H_2O. Cover slips were mounted with
444 Vectashield and sealed with nail polish.
445 Cells processed with Ki67 pA-DamID were first incubated with an antibody against
446 Ki67 (1:1000, Abcam ab15580, rabbit), and then with ^{m6}A-Tracer protein (1:500, 1.15
447 mg/mL) and an Alexa594-fused antibody against rabbit (1:250, Jackson 711-585-152,
448 donkey). Cells that received the osmotic shock or actinomycin D were first incubated with
449 antibodies against MKI67IP (1:500, Human Protein Atlas AMAB90961, mouse) and Ki67
450 (1:1000, Abcam ab15580, rabbit), and then with an Alexa488-fused antibody against mouse
451 (1:1000, ThermoFisher A11001, mouse) and an Alexa594-fused antibody against rabbit

452 (1:250, Jackson 711-585-152, donkey). HCT116 Ki67-miniAID-mClover cells were first
453 incubated with an antibody against Ki67 (1:1000, Abcam ab15580, rabbit), and then an
454 Alexa594-fused antibody against rabbit (1:250, Jackson 711-585-152, donkey).
455 Single 1,024 × 1,024 pixel confocal sections around the middle plane of nuclei were
456 imaged on a Leica SP5 with a 63× NA 1.47 oil immersion objective, using bidirectional
457 scanning, and 8× line averaging. An additional 3× electronic zoom was used for images that
458 required a higher magnification. Alternatively, z-stacks were imaged using 2x line averaging
459 and a 380 nm step size.
460
461 ***Computational analyses***
462
463 **pA-DamID processing**
464 pA-DamID reads were filtered to contain the DpnI adapter sequence, which was then
465 trimmed off with cutadapt 1.11 and custom scripts. The remaining genomic DNA sequence
466 was mapped to a hybrid genome consisting of GRCh38 v15 (without alternative haplotypes)
467 and a ribosomal model (GenBank: U13369.1) with bwa mem 0.7.17. Further data processing
468 was performed with custom R scripts. Reads were filtered to have a mapping quality of at
469 least 10 and overlap with the ends of a GATC fragment, and subsequently counted in
470 genomic bins of different sizes. In this manuscript, 50 kb genomic bins were used as a
471 compromise between resolution and reproducibility of Ki67 interaction profiles.
472 Counts were normalized to 1 million reads and a $\log_2$-ratio was calculated over the
473 Dam control sample. At least two biological replicates were generated for each condition,
474 which ratios were averaged for downstream analyses. For quantitative comparisons, the
475 $\log_2$-ratios were converted to z-scores to account for differences in dynamic range between
476 conditions and replicates [24].
477
478 **Repli-seq**
479 Adapters and low-quality reads were removed from Repli-seq reads with fastp 0.12.2 [62].
480 Trimmed reads were mapped and processed as pA-DamID reads with several differences.
481 First, duplicated reads were removed. Second, reads were not required to overlap with the
482 ends of GATC fragments. Third, $\log_2$-ratios of early/late were quantile normalized instead of
483 z-score normalization.
484
485 **RNA-seq**
486 Adapter sequences and low-quality reads were removed from RNA-seq reads with fastp
487 0.12.2 [62]. Trimmed reads were aligned to GRCh38 v15 and counted in gencode v24 genes
488 with STAR 2.5.4a [63]. DESeq2 1.30.1 was used to call differentially expressed genes [64],
489 which we defined as genes that have a Benjamini-Hochberg corrected p-value lower than
490 0.05 when testing for a $\log_2$-fold change different than 0. FPKM values were calculated with
491 `fpkm()` in DESeq2 using the combined exon length as gene length. The mean FPKM value
492 between replicates was used for downstream analyses.
493

494 **Image analysis**
495 Image analysis was performed with custom ImageJ 2.0.0 and R scripts.
496 To calculate ^{m6}A-Tracer enrichment around nucleoli, individual nuclei were first
497 segmented using the DAPI signal. This was done using a sequence of noise filtering
498 (Gaussian blur, radius of 2 pixels), contrast enhancement (0.2% saturated pixels) and
499 segmentation (Otsu method), after which a watershed algorithm was used to separate
500 closely positioned nuclei. Nuclei positioned at image borders and with abnormal dimensions
501 (due to faulty segmentation) were removed. Ki67 antibody signal was noise-filtered
502 (Gaussian blur, radius of 2 pixels), background-subtracted (rolling ball radius of 500 pixels)
503 and contrast enhanced up to 0.1% saturated pixels. These images were then used to
504 segment Ki67 domains (that we interpret as nucleoli) using a fixed threshold of 180 (of 255).
505 Any holes were filled. The segmented domains were used to calculate distance masks from
506 and into Ki67 domains. For every nucleus, distance maps were overlayed with blurred and
507 background subtracted signals for ^{m6}A-Tracer and Ki67 antibody signals, and per distance
508 group a $\log_2$-ratio was calculated over the average nuclear intensity. Finally, nuclei were
509 filtered to have reasonable enrichment scores, which removes cells with faulty segmentation
510 and mitotic cells. Average signal traces were shown for individual nuclei, and averaged
511 between all nuclei of a particular experimental condition.
512 To calculate Ki67 depletion efficiency in HCT116 Ki67-AID cells for the two additional
513 Ki67 antibodies (Novus and HPA), individual nuclei were segmented as described above.
514 Ki67 antibody and mClover signals were noise-filtered (Gaussian blur, radius of 2 pixels),
515 median-smoothed (radius of 3 pixels) and background subtracted (rolling window of 250
516 pixels). Average signals were calculated for every nucleus. For the initial Ki67 antibody
517 (Abcam), 3D stacks were imaged rather than sections through the middle plane. Image
518 analysis was performed as for the 2D slices, but using 3D implementations instead. 3D
519 Gaussian blurring was performed with a radius of 1 pixel in every direction.
520
521 **Centromere definition**
522 Locations of centromeres were downloaded from the UCSC table browser (group: mapping
523 and sequencing; track: centromeres).
524
525 **External data**
526 **Supplementary Table 1** lists the external data sets that have been used in this study.
527 Previously generated pA-DamID reads were used from the 4DN data repository
528 (https://data.4dnucleome.org/) and processed as described above. These data sets are
529 included in the processed data files that can be found in the GEO repository linked below.
530 Processed Repli-seq data in 5 kb bins was downloaded from the 4DN data repository and
531 the average score was calculated for 50 kb bins as described above. RNA-seq reads were
532 downloaded from multiple references and used to calculate average FPKM values as
533 described above.
534

535 **Data availability**
536 Data sets, computational code and lab journal entries that have been produced for this study
537 are available in the following repositories:
538 - Data generated in this manuscript: GEO data repository (GSE186206)
539 - Computer scripts: will be made available
540 - Lab journal records: will be made available
541
542
543 **ACKNOWLEDGEMENTS**
544 We thank Masatoshi Takagi for the HCT116 Ki67-AID cell line, and the NKI Digital
545 Microscopy, Flow Cytometry, Genomics, Protein Production, and RHPC core facilities for
546 technical assistance. We thank members of the BvS lab; Andrew Belmont and other
547 members of the 4D Nucleome Center for Nuclear Cytomics for helpful suggestions.
548 Supported by NIH Common Fund "4D Nucleome" Program grant U54 DK107965 (BvS,
549 DMG), ERC Advanced Grant 694466 (BvS), MSCA/AIRC iCARE2.0 fellowship 800924
550 (SGM), and Marie Curie Fellowship 838555 (SGM). The Oncode Institute is partly supported
551 by KWF Dutch Cancer Society.
552
553
554 **AUTHOR CONTRIBUTIONS**
555 TvS: Conceived and designed study, conducted majority of experiments and all data
556 analysis, wrote manuscript. SGM: Performed experiments. AV: Performed Repli-seq
557 experiments. DMG: Supervised project. BvS: Designed study, wrote manuscript, supervised
558 project.
559
560
561 **CONFLICT OF INTEREST**
562 The authors declare no conflicting interests.
563
564

565 **REFERENCES**

566

567 1. Scholzen, T. and J. Gerdes, *The Ki-67 protein: from the known and the unknown.* J
568 Cell Physiol, 2000. **182**(3): p. 311-22.
569 2. Sun, X. and P.D. Kaufman, *Ki-67: more than a proliferation marker.* Chromosoma,
570 2018. **127**(2): p. 175-186.
571 3. Remnant, L., et al., *The intrinsically disorderly story of Ki-67.* Open Biol, 2021. **11**(8):
572 p. 210120.
573 4. Verheijen, R., et al., *Ki-67 detects a nuclear matrix-associated proliferation-related*
574 *antigen. II. Localization in mitotic cells and association with chromosomes.* J Cell Sci,
575 1989. **92 (Pt 4)**: p. 531-40.
576 5. Booth, D.G., et al., *Ki-67 is a PP1-interacting protein that organises the mitotic*
577 *chromosome periphery.* Elife, 2014. **3**: p. e01641.
578 6. Cuylen, S., et al., *Ki-67 acts as a biological surfactant to disperse mitotic*
579 *chromosomes.* Nature, 2016. **535**(7611): p. 308-12.
580 7. Takagi, M., et al., *Perichromosomal protein Ki67 supports mitotic chromosome*
581 *architecture.* Genes Cells, 2016. **21**(10): p. 1113-1124.
582 8. Cuylen-Haering, S., et al., *Chromosome clustering by Ki-67 excludes cytoplasm*
583 *during nuclear assembly.* Nature, 2020. **587**(7833): p. 285-290.
584 9. Ochs, R.L., et al., *Nucleologenesis: composition and fate of prenucleolar bodies.*
585 Chromosoma, 1985. **92**(5): p. 330-6.
586 10. Dundr, M., T. Misteli, and M.O. Olson, *The dynamics of postmitotic reassembly of the*
587 *nucleolus.* J Cell Biol, 2000. **150**(3): p. 433-46.
588 11. Savino, T.M., et al., *Nucleolar assembly of the rRNA processing machinery in living*
589 *cells.* J Cell Biol, 2001. **153**(5): p. 1097-110.
590 12. Carron, C., et al., *Post-mitotic dynamics of pre-nucleolar bodies is driven by pre-*
591 *rRNA processing.* J Cell Sci, 2012. **125**(Pt 19): p. 4532-42.
592 13. Ohno, S., W.D. Kaplan, and R. Kinosita, *The centromeric and nucleolus-associated*
593 *heterochromatin of Rattus norvegicus.* Exp Cell Res, 1959. **16**(2): p. 348-57.
594 14. Lima-De-Faria, A. and J. Reitalu, *Heterochromatin in human male leukocytes.* J Cell
595 Biol, 1963. **16**: p. 315-22.
596 15. Guelen, L., et al., *Domain organization of human chromosomes revealed by mapping*
597 *of nuclear lamina interactions.* Nature, 2008. **453**(7197): p. 948-51.
598 16. van Koningsbruggen, S., et al., *High-resolution whole-genome sequencing reveals*
599 *that specific chromatin domains from most human chromosomes associate with*
600 *nucleoli.* Mol Biol Cell, 2010. **21**(21): p. 3735-48.
601 17. Dillinger, S., T. Straub, and A. Nemeth, *Nucleolus association of chromosomal*
602 *domains is largely maintained in cellular senescence despite massive nuclear*
603 *reorganisation.* PLoS One, 2017. **12**(6): p. e0178821.
604 18. Vertii, A., et al., *Two contrasting classes of nucleolus-associated domains in mouse*
605 *fibroblast heterochromatin.* Genome Res, 2019. **29**(8): p. 1235-1249.
606 19. Kind, J., et al., *Single-cell dynamics of genome-nuclear lamina interactions.* Cell,
607 2013. **153**(1): p. 178-92.
608 20. Ragoczy, T., et al., *Functional redundancy in the nuclear compartmentalization of the*
609 *late-replicating genome.* Nucleus, 2014. **5**(6): p. 626-35.
610 21. Solovei, I., et al., *LBR and lamin A/C sequentially tether peripheral heterochromatin*
611 *and inversely regulate differentiation.* Cell, 2013. **152**(3): p. 584-98.
612 22. Sobecki, M., et al., *The cell proliferation antigen Ki-67 organises heterochromatin.*
613 Elife, 2016. **5**: p. e13722.
614 23. Matheson, T.D. and P.D. Kaufman, *The p150N domain of chromatin assembly factor-*
615 *1 regulates Ki-67 accumulation on the mitotic perichromosomal layer.* Mol Biol Cell,
616 2017. **28**(1): p. 21-29.
617 24. van Schaik, T., et al., *Cell cycle dynamics of lamina-associated DNA.* EMBO Rep,
618 2020. **21**(11): p. e50636.

619 25. Greil, F., C. Moorman, and B. van Steensel, *DamID: mapping of in vivo protein-*
620 *genome interactions using tethered DNA adenine methyltransferase.* Methods
621 Enzymol, 2006. **410**: p. 342-59.
622 26. Bolzer, A., et al., *Three-dimensional maps of all chromosomes in human male*
623 *fibroblast nuclei and prometaphase rosettes.* PLoS Biol, 2005. **3**(5): p. e157.
624 27. Su, J.H., et al., *Genome-Scale Imaging of the 3D Organization and Transcriptional*
625 *Activity of Chromatin.* Cell, 2020. **182**(6): p. 1641-1659 e26.
626 28. Nemeth, A. and I. Grummt, *Dynamic regulation of nucleolar architecture.* Curr Opin
627 Cell Biol, 2018. **52**: p. 105-111.
628 29. Zhang, L.F., K.D. Huynh, and J.T. Lee, *Perinucleolar targeting of the inactive X*
629 *during S phase: evidence for a role in the maintenance of silencing.* Cell, 2007.
630 **129**(4): p. 693-706.
631 30. Sun, X., et al., *Ki-67 Contributes to Normal Cell Cycle Progression and Inactive X*
632 *Heterochromatin in p21 Checkpoint-Proficient Human Cells.* Mol Cell Biol, 2017.
633 **37**(17).
634 31. Zatsepina, O.V., et al., *Experimental induction of prenucleolar bodies (PNBs) in*
635 *interphase cells: interphase PNBs show similar characteristics as those typically*
636 *observed at telophase of mitosis in untreated cells.* Chromosoma, 1997. **105**(7-8): p.
637 418-30.
638 32. Perry, R.P. and D.E. Kelley, *Inhibition of RNA synthesis by actinomycin D:*
639 *characteristic dose-response of different RNA species.* J Cell Physiol, 1970. **76**(2): p.
640 127-39.
641 33. Politz, J.C.R., D. Scalzo, and M. Groudine, *The redundancy of the mammalian*
642 *heterochromatic compartment.* Curr Opin Genet Dev, 2016. **37**: p. 1-8.
643 34. Bizhanova, A. and P.D. Kaufman, *Close to the edge: Heterochromatin at the*
644 *nucleolar and nuclear peripheries.* Biochim Biophys Acta Gene Regul Mech, 2021.
645 **1864**(1): p. 194666.
646 35. Marchal, C., J. Sima, and D.M. Gilbert, *Control of DNA replication timing in the 3D*
647 *genome.* Nat Rev Mol Cell Biol, 2019. **20**(12): p. 721-737.
648 36. Dekker, J., et al., *The 4D nucleome project.* Nature, 2017. **549**(7671): p. 219-226.
649 37. Marchal, C., et al., *Genome-wide analysis of replication timing by next-generation*
650 *sequencing with E/L Repli-seq.* Nat Protoc, 2018. **13**(5): p. 819-839.
651 38. Reddy, K.L., et al., *Transcriptional repression mediated by repositioning of genes to*
652 *the nuclear lamina.* Nature, 2008. **452**(7184): p. 243-7.
653 39. Hiratani, I., et al., *Global reorganization of replication domains during embryonic stem*
654 *cell differentiation.* PLoS Biol, 2008. **6**(10): p. e245.
655 40. van Steensel, B. and A.S. Belmont, *Lamina-Associated Domains: Links with*
656 *Chromosome Architecture, Heterochromatin, and Gene Repression.* Cell, 2017.
657 **169**(5): p. 780-791.
658 41. Mrouj, K., et al., *Ki-67 regulates global gene expression and promotes sequential*
659 *stages of carcinogenesis.* Proc Natl Acad Sci U S A, 2021. **118**(10).
660 42. Garwain, O., et al., *The chromatin-binding domain of Ki-67 together with p53 protects*
661 *human chromosomes from mitotic damage.* bioRxiv, 2020: p. 2020.10.16.342352.
662 43. Gerdes, J., et al., *Cell cycle analysis of a cell proliferation-associated human nuclear*
663 *antigen defined by the monoclonal antibody Ki-67.* J Immunol, 1984. **133**(4): p. 1710-
664 5.
665 44. Stenstrom, L., et al., *Mapping the nucleolar proteome reveals a spatiotemporal*
666 *organization related to intrinsic protein disorder.* Mol Syst Biol, 2020. **16**(8): p. e9469.
667 45. Saiwaki, T., et al., *In vivo dynamics and kinetics of pKi-67: transition from a mobile to*
668 *an immobile form at the onset of anaphase.* Exp Cell Res, 2005. **308**(1): p. 123-34.
669 46. Crabbe, L., et al., *Human telomeres are tethered to the nuclear envelope during*
670 *postmitotic nuclear assembly.* Cell Rep, 2012. **2**(6): p. 1521-9.
671 47. Dechat, T., et al., *LAP2alpha and BAF transiently localize to telomeres and specific*
672 *regions on chromatin during nuclear assembly.* J Cell Sci, 2004. **117**(Pt 25): p. 6117-
673 28.

674 48. MacCallum, D.E. and P.A. Hall, *Biochemical characterization of pKi67 with the*
675 *identification of a mitotic-specific form associated with hyperphosphorylation and*
676 *altered DNA binding.* Exp Cell Res, 1999. **252**(1): p. 186-98.
677 49. Bridger, J.M., I.R. Kill, and P. Lichter, *Association of pKi-67 with satellite DNA of the*
678 *human genome in early G1 cells.* Chromosome Res, 1998. **6**(1): p. 13-24.
679 50. Quinodoz, S.A., et al., *Higher-Order Inter-chromosomal Hubs Shape 3D Genome*
680 *Organization in the Nucleus.* Cell, 2018. **174**(3): p. 744-757 e24.
681 51. MacCallum, D.E. and P.A. Hall, *The biochemical characterization of the DNA binding*
682 *activity of pKi67.* J Pathol, 2000. **191**(3): p. 286-98.
683 52. Luderus, M.E., et al., *Binding of matrix attachment regions to lamin polymers involves*
684 *single-stranded regions and the minor groove.* Mol Cell Biol, 1994. **14**(9): p. 6297-
685 305.
686 53. Meuleman, W., et al., *Constitutive nuclear lamina-genome interactions are highly*
687 *conserved and associated with A/T-rich sequence.* Genome Res, 2013. **23**(2): p.
688 270-80.
689 54. Sobecki, M., et al., *Cell-Cycle Regulation Accounts for Variability in Ki-67 Expression*
690 *Levels.* Cancer Res, 2017. **77**(10): p. 2722-2734.
691 55. Miller, I., et al., *Ki67 is a Graded Rather than a Binary Marker of Proliferation versus*
692 *Quiescence.* Cell Rep, 2018. **24**(5): p. 1105-1112 e5.
693 56. Bloom, K. and V. Costanzo, *Centromere Structure and Function.* Prog Mol Subcell
694 Biol, 2017. **56**: p. 515-539.
695 57. Barra, V. and D. Fachinetti, *The dark side of centromeres: types, causes and*
696 *consequences of structural abnormalities implicating centromeric DNA.* Nat
697 Commun, 2018. **9**(1): p. 4340.
698 58. Bury, L., et al., *Alpha-satellite RNA transcripts are repressed by centromere-*
699 *nucleolus associations.* Elife, 2020. **9**.
700 59. Giunta, S., et al., *CENP-A chromatin prevents replication stress at centromeres to*
701 *avoid structural aneuploidy.* Proc Natl Acad Sci U S A, 2021. **118**(10).
702 60. Vogel, M.J., D. Peric-Hupkes, and B. van Steensel, *Detection of in vivo protein-DNA*
703 *interactions using DamID in mammalian cells.* Nat Protoc, 2007. **2**(6): p. 1467-78.
704 61. Leemans, C., et al., *Promoter-Intrinsic and Local Chromatin Features Determine*
705 *Gene Repression in LADs.* Cell, 2019. **177**(4): p. 852-864 e14.
706 62. Chen, S., et al., *fastp: an ultra-fast all-in-one FASTQ preprocessor.* Bioinformatics,
707 2018. **34**(17): p. i884-i890.
708 63. Dobin, A., et al., *STAR: ultrafast universal RNA-seq aligner.* Bioinformatics, 2013.
709 **29**(1): p. 15-21.
710 64. Love, M.I., W. Huber, and S. Anders, *Moderated estimation of fold change and*
711 *dispersion for RNA-seq data with DESeq2.* Genome Biol, 2014. **15**(12): p. 550.
712 65. Consortium, E.P., *An integrated encyclopedia of DNA elements in the human*
713 *genome.* Nature, 2012. **489**(7414): p. 57-74.
714 66. Kelso, T.W.R., et al., *Chromatin accessibility underlies synthetic lethality of SWI/SNF*
715 *subunits in ARID1A-mutant cancers.* Elife, 2017. **6**.
716 67. Dai, Z., et al., *Methionine metabolism influences genomic architecture and gene*
717 *expression through H3K4me3 peak width.* Nat Commun, 2018. **9**(1): p. 1955.
718 68. Slaats, G.G., et al., *Screen-based identification and validation of four new ion*
719 *channels as regulators of renal ciliogenesis.* J Cell Sci, 2015. **128**(24): p. 4550-9.
720 69. Durrbaum, M., et al., *The deregulated microRNAome contributes to the cellular*
721 *response to aneuploidy.* BMC Genomics, 2018. **19**(1): p. 197.
722 70. Harenza, J.L., et al., *Transcriptomic profiling of 39 commonly-used neuroblastoma*
723 *cell lines.* Sci Data, 2017. **4**: p. 170033.
724

725 **FIGURE LEGENDS**
726
727 **Fig 1. Visualization and genome-wide profiling of DNA-Ki67 interactions using pA-**
728 **DamID**
729 **(A)** Schematic overview of pA-DamID [24]. Permeabilized cells are incubated with a primary
730 antibody (e.g. against Ki67), followed by a fusion of proteinA and Dam (pA-Dam). After
731 removal of unbound pA-Dam, the Dam enzyme is activated by addition of S-
732 adenosylmethionine (SAM), resulting in local deposition of ^{m6}A marks. ^{m6}A-marked DNA can
733 be processed for high-throughput sequencing, or alternatively cells can be fixed and ^{m6}A
734 marks visualized using the ^{m6}A-Tracer protein.
735 **(B)** Representative confocal microscopy sections of HCT116 cells following pA-DamID with
736 free Dam (top panel) or Ki67 antibody (bottom panel), labeled with ^{m6}A-Tracer protein and
737 stained for Ki67. Scale bar: 5 μm.
738 **(C)** Quantification of the enrichment of Ki67 antibody and ^{m6}A-Tracer signals relative to
739 segmented Ki67 domains (that we interpret as nucleoli) in different cell lines. For every cell,
740 the enrichment is calculated by pixel-distances relative to the mean signal of that cell, and
741 represented as a $\log_2$-ratio. Negative distances are outside of Ki67 domains, a distance of
742 zero marks the domain boundary and positive distances are inside of Ki67 domains. Every
743 thin line corresponds to an individual cell and the thick line is the mean of all cells. Results
744 are combined from three (hTERT-RPE) or one (HCT116 and K562) biological replicates.
745 **(D)** Comparison of Ki67 pA-DamID profiles ($\log_2$-ratios over the free Dam control) across two
746 chromosomes in hTERT-RPE, HCT116 and K562 cells. Sequenced reads are counted and
747 normalized in 50 kb bins. Data are averages of *n* biological replicates and smoothed with a
748 running mean across nine 50 kb bins for visualization purposes. Centromeres are
749 highlighted by black bars.
750 **(E)** Distributions of Ki67 interactions for all chromosomes, ordered by decreasing
751 chromosome size. rDNA-containing chromosomes are highlighted by black borders.
752 Boxplots: horizontal lines represent 25th, 50th, and 75th percentiles; whiskers extend to 5th
753 and 95th percentiles.
754 **(F)** Distributions of Ki67 interactions nearby centromeres. Boxplots are drawn for every 0.5
755 Mb, following the specification as in (E) with the 50th percentile highlighted in red.
756 **(G)** The mean Ki67 interaction score near centromeres is plotted for each chromosome
757 ordered by size (within 2Mb of centromeres, overlapping the enrichment in (F)). rDNA-
758 containing chromosomes are highlighted in red.
759
760 **Fig 2. Cell cycle dynamics of Ki67 interactions**
761 **(A)** Representative confocal microscopy sections of hTERT-RPE cells processed with Ki67
762 pA-DamID, following synchronization with a mitotic shake-off (t = 0 h, see Methods) and time
763 points after replating of the synchronized cells. Cells were stained for Ki67 and labeled with
764 ^{m6}A-Tracer protein. Scale bar: 5 μm.
765 **(B)** Quantification of ^{m6}A-Tracer and Ki67 antibody enrichment near Ki67 domains
766 (interpreted as PNBs / nucleoli) in synchronized hTERT-RPE cells, as described in (**Fig 1C**).

767 Instead of individual cell traces, the 95%-confidence interval of the mean is added as shaded
768 area. Results are combined from three (unsynchronized cells) or one (synchronized cells)
769 biological replicates.
770 **(C)** Ki67 interactions profiles for the synchronized hTERT-RPE cells. Two representative
771 chromosomes were visualized to highlight the differences between large (chr2) and small
772 chromosomes (chr22). Log_2-ratios were converted to z-scores to correct for differences in
773 dynamic range between conditions and replicates. Data profiles are averages of *n*
774 experiments and smoothed with a running mean across nine 50 kb bins. Centromeres are
775 highlighted by black bars.
776 **(D)** Smooth loess curves of Ki67 interactions plotted against the distance to chromosome
777 ends for cells synchronized in metaphase (t = 0 h). Lines represent individual chromosomes.
778 **(E)** Chromosomal distributions of genome-wide differences between Ki67 interactions in
779 early G1 (t = 1 h) and unsynchronized cells. Boxplots: horizontal lines represent 25th, 50th,
780 and 75th percentiles; whiskers extend to 5th and 95th percentiles.
781 **(F)** Mean chromosomal differences in Ki67 interaction scores between interphase time
782 points and early G1 cells (t = 1 h) are plotted for chromosomes sorted by size.
783
784 **Fig 3. Ki67 interactions are restricted by nucleolar positioning**
785 **(A)** Representative confocal microscopy sections of hTERT-RPE cells following 3 hours of a
786 low dose of actinomycin D (ActD, 50 ng/mL in 0.05% dimethyl sulfoxide (DMSO)) to disrupt
787 nucleoli, and of cells treated with a similar quantity of DMSO as control. Cells were stained
788 for MKI67IP and Ki67 proteins to visualize nucleolar disruption and new Ki67 localization
789 patterns. Scale bar: 10 μm.
790 **(B)** Comparison of Ki67 interactions in the three cell lines after ActD-induced nucleolar
791 disruption for two representative chromosomes. DMSO control and ActD treated cells are
792 shown in red and blue, respectively. Data are averages of two experiments and smoothed
793 with a running mean across nine 50 kb bins for visualization. Centromeres are highlighted by
794 black bars.
795 **(C)** The differences between ActD and control conditions in mean chromosomal Ki67 signal
796 is plotted for chromosomes sorted by size. rDNA-containing chromosomes are highlighted
797 with triangles.
798 **(D)** The difference between ActD and control conditions in mean Ki67 interactions scores
799 near centromeres is plotted for each chromosome (within 2Mb of centromeres, overlapping
800 the enrichment in (**Fig 1F**)). rDNA-containing chromosomes are highlighted in red.
801
802 **Fig 4. Ki67 and Lamin B1 together mark the late-replicating genome**
803 **(A)** Comparison of Ki67 interactions with Lamin B1 interactions (both log_2-ratios) and DNA
804 replication timing (Repli-seq log_2-ratio of Early/Late) for a representative genomic region.
805 Orange arrows highlight domains with high Ki67 and generally low Lamin B1 interactions,
806 and vice-versa. Data profiles are averages of *n* experiments and smoothed with a running
807 mean across nine 50 kb bins. Centromeres are highlighted by black bars.

808 **(B)** Binned scatterplots between Ki67 and Lamin B1 interactions (log_2-ratios), showing the
809 amount of genomic 50kb bins overlapping these points (top panels) and the mean replication
810 timing score of overlapping genomic bins (log_2 Early/Late) (bottom panels). Points are only
811 shown with at least 10 overlapping genomic bins for a robust estimation of mean scores. A
812 separate color bar is used for replication timing in K562 cells, which have a reduced dynamic
813 range. Replication timing data were obtained from the 4D Nucleome data repository [36].
814
815 **Fig 5. Effects of Ki67 depletion on Lamin B1 interactions and replication timing**
816 **(A)** Overview of the Ki67 depletion experiment in HCT116 Ki67-AID cells (top). Cells were
817 either cultured with a double thymidine arrest to enrich for S-phase cells (which includes one
818 cell division) or arrested in G2 by CDK1 inhibition immediately following an initial S-phase
819 arrest (which prevents a cell division). FACS analysis confirmed successful synchronization
820 and illustrates that Ki67 depletion does not affect this (bottom panels).
821 **(B)** Differences in mean Ki67 chromosome scores between S- and G2-synchronized
822 HCT116 Ki67-AID cells.
823 **(C)** Representative genomic region showing the effect of Ki67 depletion on Lamin B1
824 interactions, for HCT116 Ki67-AID cells synchronized in S-phase (left panel) and G2-phase
825 (right panel). Black and red lines represent conditions with normal and depleted Ki67 levels,
826 respectively. Ki67 interactions were only profiled at non-depleted levels. Orange arrows
827 highlight regions with high Ki67 interactions that gain Lamin B1 interactions upon Ki67
828 depletion. Data profiles are averages of 2 experiments and smoothed with a running mean
829 across nine 50kb bins. The centromere is located just to the right of the depicted region.
830 **(D)** Binned scatterplots of Lamin B1 interactions at in HCT116 cells with normal versus
831 depleted Ki67 levels, as described in (**Fig 4B**). Bins are colored by mean Ki67 interactions in
832 S-phase (top panels) and G2-phase (bottom panels). Signals are smoothed with a running
833 mean of three 50 kb bins to reduce noise in the data.
834 **(E)** Representative genomic region showing the effect of auxin-mediated Ki67 depletion on
835 (S-phase) Lamin B1 interactions and replication timing (log_2 Early/Late) in HCT116 Ki67-AID
836 cells, as described in (C). Orange arrows highlight domains with gained Lamin B1
837 interactions and delayed replication timing; purple arrows highlight domains with gained
838 Lamin B1 interactions but unaffected replication timing.
839 **(F)** Binned scatterplots (as in (D)) of replication timing (RT, E/L) in cells with normal versus
840 depleted Ki67 levels, colored by the density of overlapping 50 kb bins (left panel) and mean
841 Ki67 interactions at normal Ki67 levels (right panel).
842 **(G)** Distribution of differences in replication timing (RT) nearby centromeres. Boxplots:
843 horizontal lines represent 25th, 50th, and 75th percentiles; whiskers extend to 5th and 95th
844 percentiles.
845 **(H)** Mean difference in replication timing (RT) within 2 Mb from the centromere of each
846 chromosome. rDNA-containing chromosomes are highlighted in red.
847

848 **Fig 6. Comparison of the Ki67 and Lamin B1 balance with H3K27me3 and H3K9me3**
849 **(A)** Comparison of Ki67 interactions with Lamin B1 interactions and H3K27me3 and
850 H3K9me3 histone modifications for a representative genomic region. Data profiles are
851 averages of *n* pA-DamID experiments and smoothed with a running mean across 9 50kb
852 bins. Centromeres are highlighted by black bars.
853 **(B)** Binned scatterplots of Ki67 and Lamin B1 interactions as in (**Fig 4B**), colored according
854 to the mean H3K27me3 and H3K9me3 signals.
855 **(C)** A similar figure as (**Fig 5B**), but additionally showing the effect of Ki67 depletion on
856 H3K27me3 and H3K9me3.
857 **(D)** Similar plots as (**Fig 5D**), but instead showing H3K27me3 and H3K9me3 at normal and
858 depleted Ki67 levels. Bins are colored by the Ki67 interactions in cells with normal Ki67
859 levels.
860
861
862 **SUPPLEMENTARY FIGURE LEGENDS**
863
864 **Fig S1. Additional information and controls for Ki67 pA-DamID**
865 **(A)** Example of raw Ki67 pA-DamID profiles for a representative experiment in HCT116 cells.
866 ^{m6}A-marked DNA is specifically amplified, sequenced, counted in 50 kb bins and counts-per-
867 million normalized (cpm) for Ki67 (top profile) and free Dam (middle profile). A $\log_2$-ratio
868 between Ki67 and Dam accounts for DNA accessibility and amplification bias, and is used as
869 a measure of Ki67 interactions. Data profiles are smoothed with a running mean across nine
870 50kb bins for visualization purposes. Centromeres are highlighted by red bars.
871 **(B)** Replicate experiment correlations for Ki67 interactions ($\log_2$-ratios) measured in
872 unsynchronized HCT116 cells (top panel) and K562 cells (bottom panel).
873 **(C)** Overview of Pearson correlations between replicate experiments for all experimental
874 conditions studied throughout this manuscript, separated by cell line and including
875 perturbation experiments.
876 **(D)** Representative maximum projections of confocal microscopy stacks of HCT116 Ki67-
877 miniAID-mClover cells (HCT116 Ki67-AID in short) with normal (top panels) and auxin-
878 mediated depleted Ki67 levels (bottom panels). Ki67 levels were visualized directly by
879 mClover fluorescence, and indirectly by immunofluorescence with a Ki67 antibody. Scale
880 bar: 10 μm.
881 **(E)** Quantification of Ki67 levels measured by mClover (middle panel) and immunostaining
882 (bottom panel) from three independent replicates. Every point represents a single cell.
883 **(F)** Two representative chromosomes showing the effect of auxin-mediated Ki67 depletion in
884 HCT116 Ki67-AID cells on Ki67 interactions as measured by pA-DamID. Data are averages
885 of two biological replicates and smoothed with a running mean across nine 50kb bins.
886 Centromeres are marked by red bars.
887 **(G)** Correlation of all 50 kb genomic bins from profiles described in (F).
888

889 **Fig S2. Ki67 interactions are reproducible between antibodies**
890 **(A)** Quantification of Ki67 levels as described in (**Fig S1D-E**) based on mClover and Ki67
891 immunostaining signals in HCT116 Ki67-AID cells using different Ki67 antibodies. For this
892 experiment, single confocal microscopy sections from the middle of cell nuclei were used
893 rather than maximum projections from entire nuclei. Results are combined from two
894 biological replicates.
895 **(B)** Quantification of ^{m6}A-Tracer enrichment around Ki67-marked nucleoli, as described in
896 (**Fig 1B-C**). Results are combined from one (middle-targeting antibody) or two (N- and C-
897 terminus antibodies) biological replicates. Data from **Fig 1C** are not included here.
898 **(C)** Ki67 interactions on two representative chromosomes as determined by pA-DamID using
899 three different Ki67 antibodies. Data profiles are averages of *n* biological replicates and
900 smoothed with a running mean across nine 50kb bins. Centromeres are highlighted by black
901 bars.
902 **(D-E)** Correlation of all 50 kb genomic bins between Ki67 interactions profiled with the
903 middle-targeting antibody and the N- **(D)** and C-terminus antibodies **(E)**.
904
905 **Fig S3. Ki67 interactions are more conserved on small chromosomes, and are not**
906 **enriched at rDNA repeats**
907 **(A)** Pearson correlations between cell lines along all 50 kb genomic bins of individual
908 chromosomes. The panel title indicates the first cell line and the color indicates the second
909 cell line between which the correlation was calculated.
910 **(B)** Enrichment of rDNA sequences detected by Ki67 pA-DamID compared to the Dam
911 control.
912
913 **Fig S4. A short osmotic shock recapitulates Ki67 maturation from PNBs to nucleoli**
914 **(A)** Representative confocal microscopy sections of hTERT-RPE cells before a 15-minute
915 osmotic shock (0.2x PBS) (top panels), and after 30 and 180 minutes of recovery in
916 complete medium (middle and bottom panels). Formaldehyde-fixed cells were stained for
917 MKI67IP and Ki67. Scale bar: 10 μm.
918 **(B)** Representative chromosomes showing Ki67 interactions in unsynchronized hTERT-RPE
919 cells, two interphase time points (data are the same as in **Fig 2C**) and the two time points
920 following osmotic shock. Note that the regions that change Ki67 interactions during
921 interphase show the same trends after the osmotic shock. Data profiles are averages of two
922 experiments and smoothed with a running mean across nine 50 kb bins. Centromeres are
923 highlighted by black bars.
924 **(C)** Changes in chromosomal distributions of Ki67 are similar for progression in G1 phase (x-
925 axis: difference in mean interactions per chromosome between 10h and 1h after mitosis) and
926 upon recovery from osmotic shock (y-axis: difference in mean interactions per chromosome
927 between 180 min and 30 min after termination of the osmotic shock (OS)).
928 **(D-E)** Representative confocal microscopy sections showing the effect of ActD on nucleolar
929 morphology in HCT116 **(D)** and K562 cells **(E)**, as described in (**Fig 3A**). Scale bar: 10 μm.
930

931 **Fig S5. Loss of Ki67 interactions does not correlate with gene expression changes**
932 **(A)** Bar plot showing average replication timing (log_2-ratio Early/Late) for centromeres. All
933 reads were selected that aligned to regions marked as centromeres (UCSC Table browser;
934 hg38 centromeres) regardless of their mapping quality and, following counts-per-million
935 normalization, the E/L ratio was calculated between the total centromeric counts. Between 3-
936 5% of the late-fraction mapped to centromeres.
937 **(B-C)** Similar plots as (**Fig 5G-H**), but showing differences in Lamin B1 interactions instead.
938 **(D)** Similar plot as (**Fig 4B**), but instead highlighting for every gene the expression level (in
939 log_{10} FPKM). Expression data are used from [30, 65-70] (see Methods).
940 **(E)** Scatterplot of mean gene expression (counts per million; cpm) versus expression
941 difference (log_2-fold change) following auxin-mediated Ki67 depletion in HCT116 Ki67-AID
942 cells. Significant genes (Benjamini-Hochberg adjusted p-value < 0.05) are highlighted in red.
943 **(F)** Boxplots showing Ki67 interactions for differentially expressed genes following Ki67
944 depletion in hTERT-RPE cells. Gene expression calls are from [30]. Boxplots: horizontal
945 lines represent 25th, 50th, and 75th percentiles; whiskers extend to 5th and 95th percentiles.
946

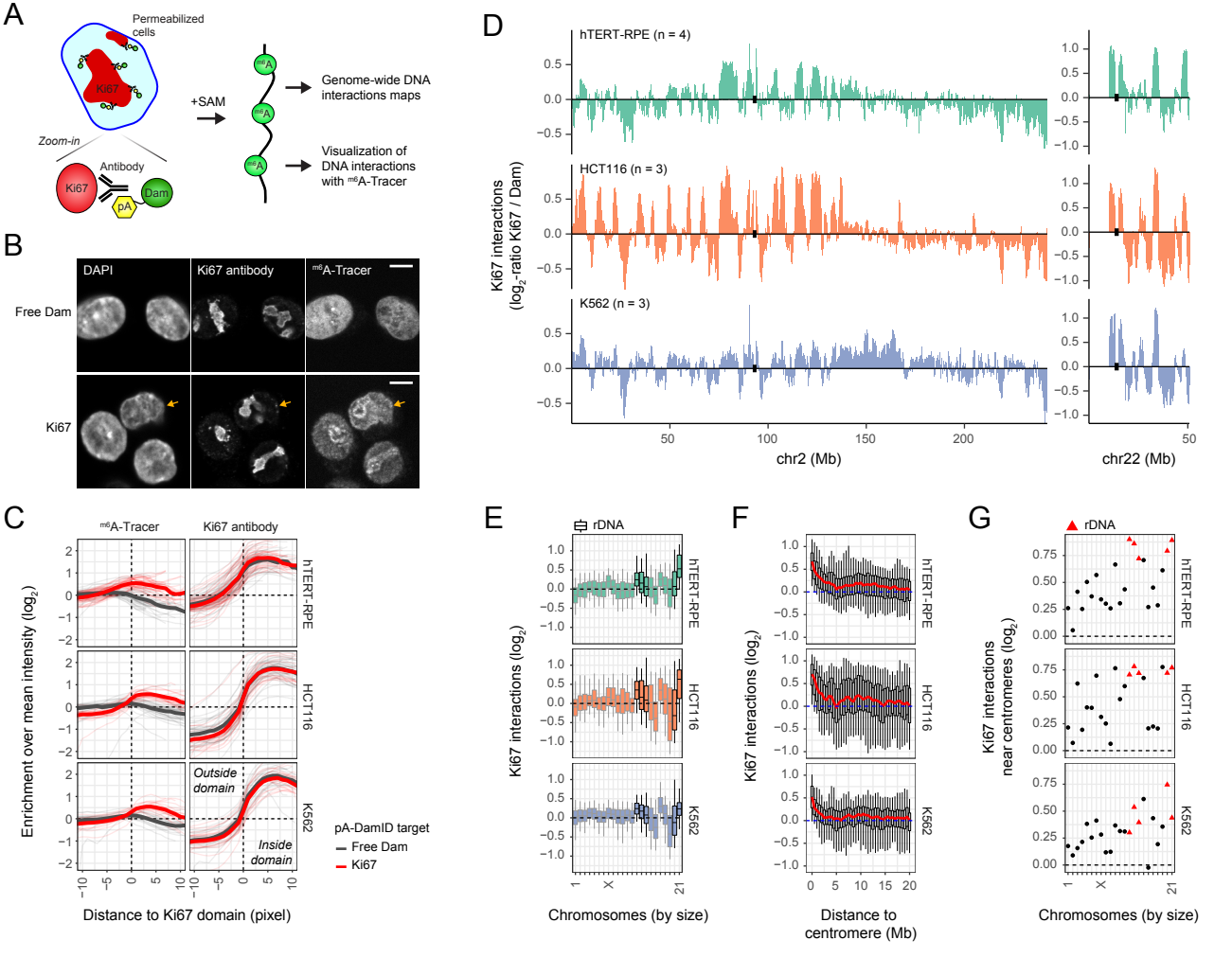

Fig 1. Visualization and genome-wide profiling of DNA-Ki67 interactions using pA-DamID

(A) Schematic overview of pA-DamID [24]. Permeabilized cells are incubated with a primary antibody (e.g. against Ki67), followed by a fusion of proteinA and Dam (pA-Dam). After removal of unbound pA-Dam, the Dam enzyme is activated by addition of S-adenosylmethionine (SAM), resulting in local deposition of m6A marks. m6A-marked DNA can be processed for high-throughput sequencing, or alternatively cells can be fixed and m6A marks visualized using the m6A-Tracer protein.
(B) Representative confocal microscopy sections of HCT116 cells following pA-DamID with free Dam (top panel) or Ki67 antibody (bottom panel), labeled with m6A-Tracer protein and stained for Ki67. Scale bar: 5 μm.
(C) Quantification of the enrichment of Ki67 antibody and m6A-Tracer signals relative to segmented Ki67 domains (that we interpret as nucleoli) in different cell lines. For every cell, the enrichment is calculated by pixel-distances relative to the mean signal of that cell, and represented as a log2-ratio. Negative distances are outside of Ki67 domains, a distance of zero marks the domain boundary and positive distances are inside of Ki67 domains. Every thin line corresponds to an individual cell and the thick line is the mean of all cells. Results are combined from three (hTERT-RPE) or one (HCT116 and K562) biological replicates.
(D) Comparison of Ki67 pA-DamID profiles (log2-ratios over the free Dam control) across two chromosomes in hTERT-RPE, HCT116 and K562 cells. Sequenced reads are counted and normalized in 50 kb bins. Data are averages of n biological replicates and smoothed with a running mean across nine 50 kb bins for visualization purposes. Centromeres are highlighted by black bars.
(E) Distributions of Ki67 interactions for all chromosomes, ordered by decreasing chromosome size. rDNA-containing chromosomes are highlighted by black borders. Boxplots: horizontal lines represent 25th, 50th, and 75th percentiles; whiskers extend to 5th and 95th percentiles.
(F) Distributions of Ki67 interactions nearby centromeres. Boxplots are drawn for every 0.5 Mb, following the specification as in (E) with the 50th percentile highlighted in red.
(G) The mean Ki67 interaction score near centromeres is plotted for each chromosome ordered by size (within 2Mb of centromeres, overlapping the enrichment in (F)). rDNA-containing chromosomes are highlighted in red.

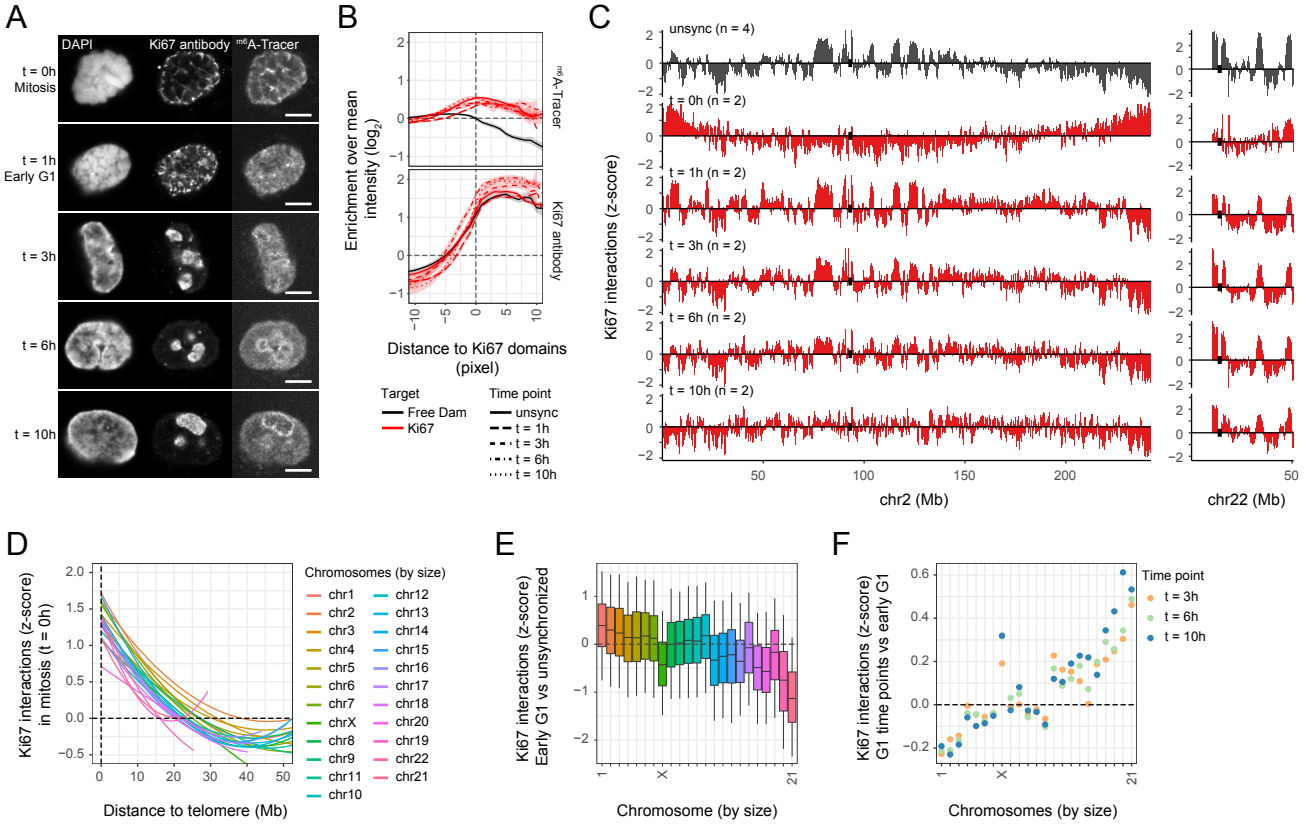

Fig 2. Cell cycle dynamics of Ki67 interactions

(A) Representative confocal microscopy sections of hTERT-RPE cells processed with Ki67 pA-DamID, following synchronization with a mitotic shake-off (t = 0 h, see Methods) and time points after replating of the synchronized cells. Cells were stained for Ki67 and labeled with m6A-Tracer protein. Scale bar: 5 µm.
(B) Quantification of m6A-Tracer and Ki67 antibody enrichment near Ki67 domains (interpreted as PNBs / nucleoli) in synchronized hTERT-RPE cells, as described in (Fig 1C). Instead of individual cell traces, the 95%-confidence interval of the mean is added as shaded area. Results are combined from three (unsynchronized cells) or one (synchronized cells) biological replicates.
(C) Ki67 interactions profiles for the synchronized hTERT-RPE cells. Two representative chromosomes were visualized to highlight the differences between large (chr2) and small chromosomes (chr22). Log2-ratios were converted to z-scores to correct for differences in dynamic range between conditions and replicates. Data profiles are averages of n experiments and smoothed with a running mean across nine 50 kb bins. Centromeres are highlighted by black bars.
(D) Smooth loess curves of Ki67 interactions plotted against the distance to chromosome ends for cells synchronized in metaphase (t = 0 h). Lines represent individual chromosomes.
(E) Chromosomal distributions of genome-wide differences between Ki67 interactions in early G1 (t = 1 h) and unsynchronized cells. Boxplots: horizontal lines represent 25th, 50th, and 75th percentiles; whiskers extend to 5th and 95th percentiles.
(F) Mean chromosomal differences in Ki67 interaction scores between interphase time points and early G1 cells (t = 1 h) are plotted for chromosomes sorted by size.

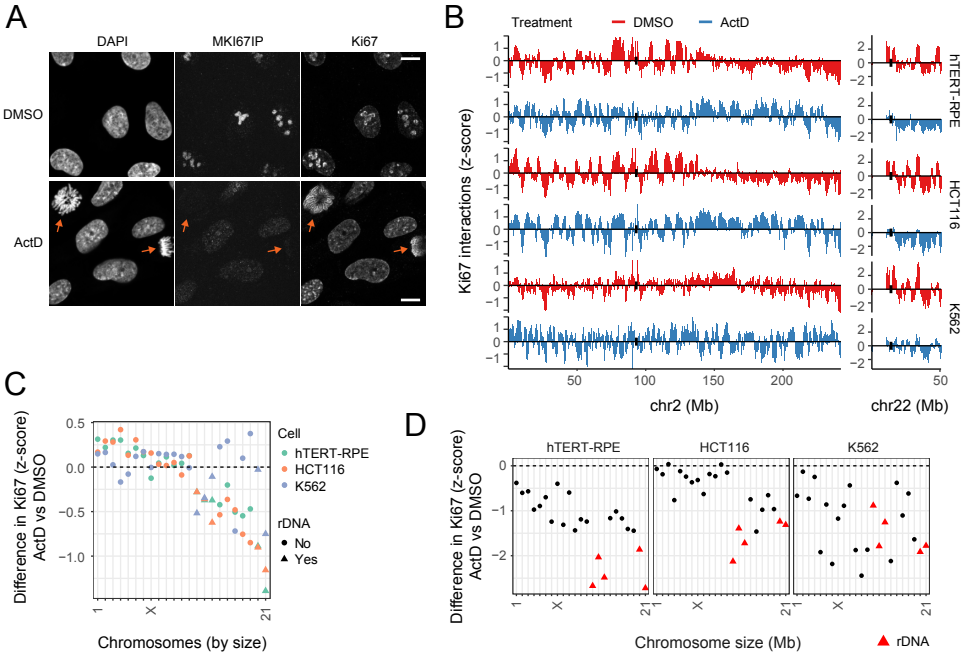

Fig 3. Ki67 interactions are restricted by nucleolar positioning

(A) Representative confocal microscopy sections of hTERT-RPE cells following 3 hours of a low dose of actinomycin D (ActD, 50 ng/mL in 0.05% dimethyl sulfoxide (DMSO)) to disrupt nucleoli, and of cells treated with a similar quantity of DMSO as control. Cells were stained for MKI67IP and Ki67 proteins to visualize nucleolar disruption and new Ki67 localization patterns. Scale bar: 10 μm.

(B) Comparison of Ki67 interactions in the three cell lines after ActD-induced nucleolar disruption for two representative chromosomes. DMSO control and ActD treated cells are shown in red and blue, respectively. Data are averages of two experiments and smoothed with a running mean across nine 50 kb bins for visualization. Centromeres are highlighted by black bars.

(C) The differences between ActD and control conditions in mean chromosomal Ki67 signal is plotted for chromosomes sorted by size. rDNA-containing chromosomes are highlighted with triangles.

(D) The difference between ActD and control conditions in mean Ki67 interactions scores near centromeres is plotted for each chromosome (within 2Mb of centromeres, overlapping the enrichment in (Fig 1F)). rDNA-containing chromosomes are highlighted in red.

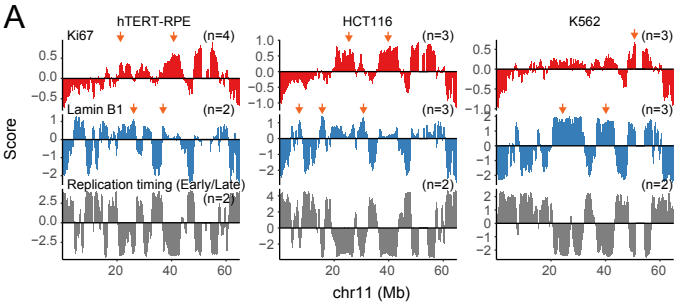

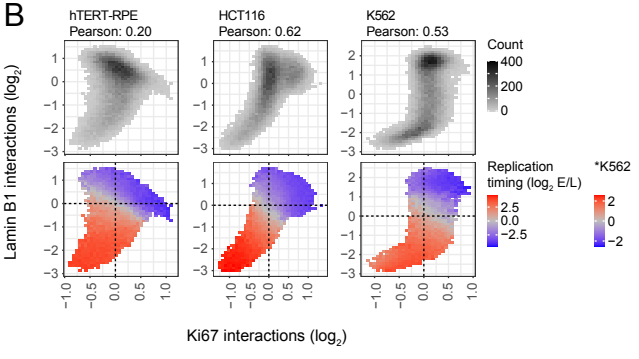

Fig 4. Ki67 and Lamin B1 together mark the late-replicating genome

(A) Comparison of Ki67 interactions with Lamin B1 interactions (both log2-ratios) and DNA replication timing (Repli-seq log2-ratio of Early/Late) for a representative genomic region. Orange arrows highlight domains with high Ki67 and generally low Lamin B1 interactions, and vice-versa. Data profiles are averages of n experiments and smoothed with a running mean across nine 50 kb bins. Centromeres are highlighted by black bars.

(B) Binned scatterplots between Ki67 and Lamin B1 interactions (log2-ratios), showing the amount of genomic 50kb bins overlapping these points (top panels) and the mean replication timing score of overlapping genomic bins (log2 Early/Late) (bottom panels). Points are only shown with at least 10 overlapping genomic bins for a robust estimation of mean scores. A separate color bar is used for replication timing in K562 cells, which have a reduced dynamic range. Replication timing data were obtained from the 4D Nucleome data repository [36].

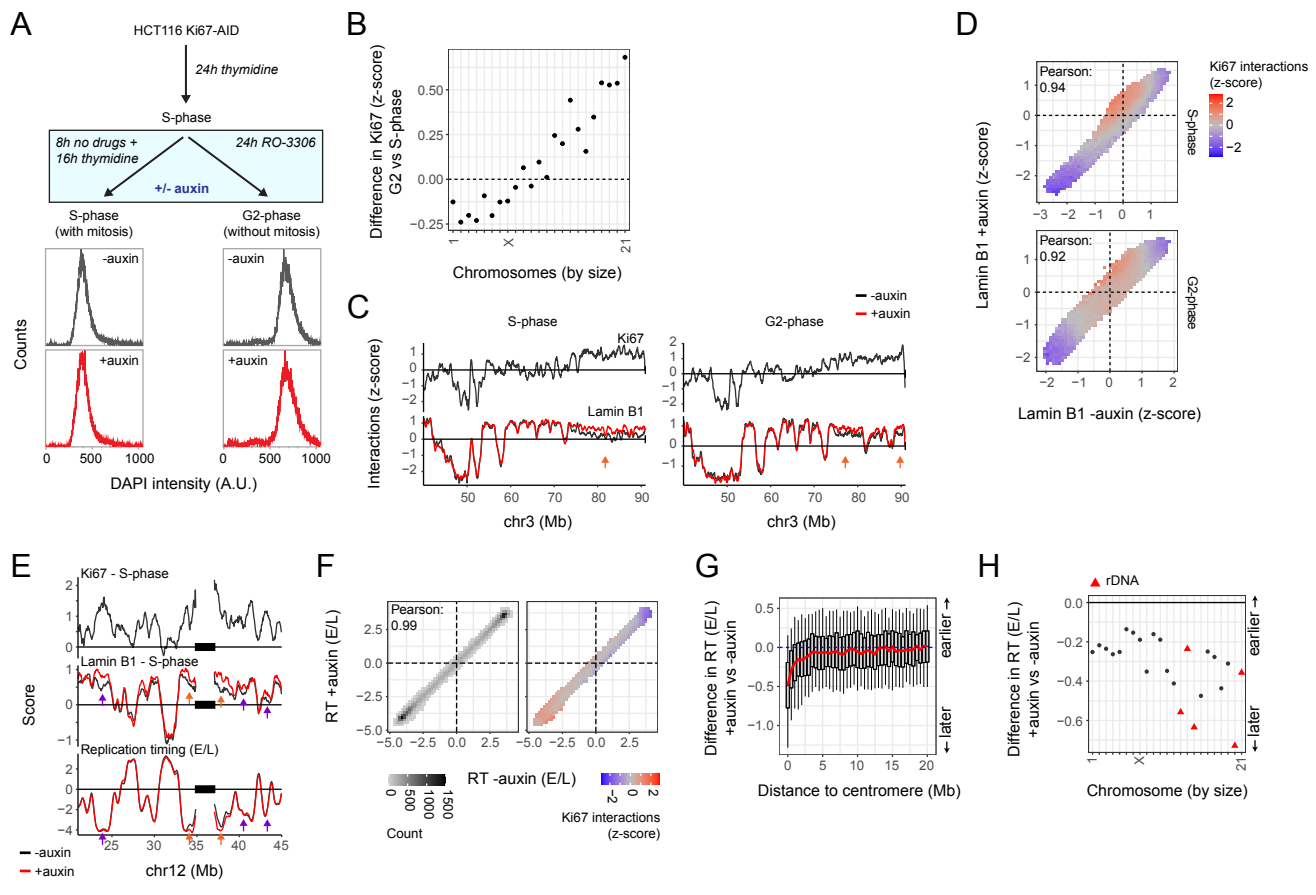

Fig 5. Effects of Ki67 depletion on Lamin B1 interactions and replication timing

(A) Overview of the Ki67 depletion experiment in HCT116 Ki67-AID cells (top). Cells were either cultured with a double thymidine arrest to enrich for S-phase cells (which includes one cell division) or arrested in G2 by CDK1 inhibition immediately following an initial S-phase arrest (which prevents a cell division). FACS analysis confirmed successful synchronization and illustrates that Ki67 depletion does not affect this (bottom panels).
(B) Differences in mean Ki67 chromosome scores between S- and G2-synchronized HCT116 Ki67-AID cells.
(C) Representative genomic region showing the effect of Ki67 depletion on Lamin B1 interactions, for HCT116 Ki67-AID cells synchronized in S-phase (left panel) and G2-phase (right panel). Black and red lines represent conditions with normal and depleted Ki67 levels, respectively. Ki67 interactions were only profiled at non-depleted levels. Orange arrows highlight regions with high Ki67 interactions that gain Lamin B1 interactions upon Ki67 depletion. Data profiles are averages of 2 experiments and smoothed with a running mean across nine 50kb bins. The centromere is located just to the right of the depicted region.
(D) Binned scatterplots of Lamin B1 interactions at in HCT116 cells with normal versus depleted Ki67 levels, as described in (Fig 4B). Bins are colored by mean Ki67 interactions in S-phase (top panels) and G2-phase (bottom panels). Signals are smoothed with a running mean of three 50 kb bins to reduce noise in the data.
(E) Representative genomic region showing the effect of auxin-mediated Ki67 depletion on (S-phase) Lamin B1 interactions and replication timing (log2 Early/Late) in HCT116 Ki67-AID cells, as described in (C). Orange arrows highlight domains with gained Lamin B1 interactions and delayed replication timing; purple arrows highlight domains with gained Lamin B1 interactions but unaffected replication timing.
(F) Binned scatterplots (as in (D)) of replication timing (RT, E/L) in cells with normal versus depleted Ki67 levels, colored by the density of overlapping 50 kb bins (left panel) and mean Ki67 interactions at normal Ki67 levels (right panel).
(G) Distribution of differences in replication timing (RT) nearby centromeres. Boxplots: horizontal lines represent 25th, 50th, and 75th percentiles; whiskers extend to 5th and 95th percentiles.
(H) Mean difference in replication timing (RT) within 2 Mb from the centromere of each chromosome. rDNA-containing chromosomes are highlighted in red.

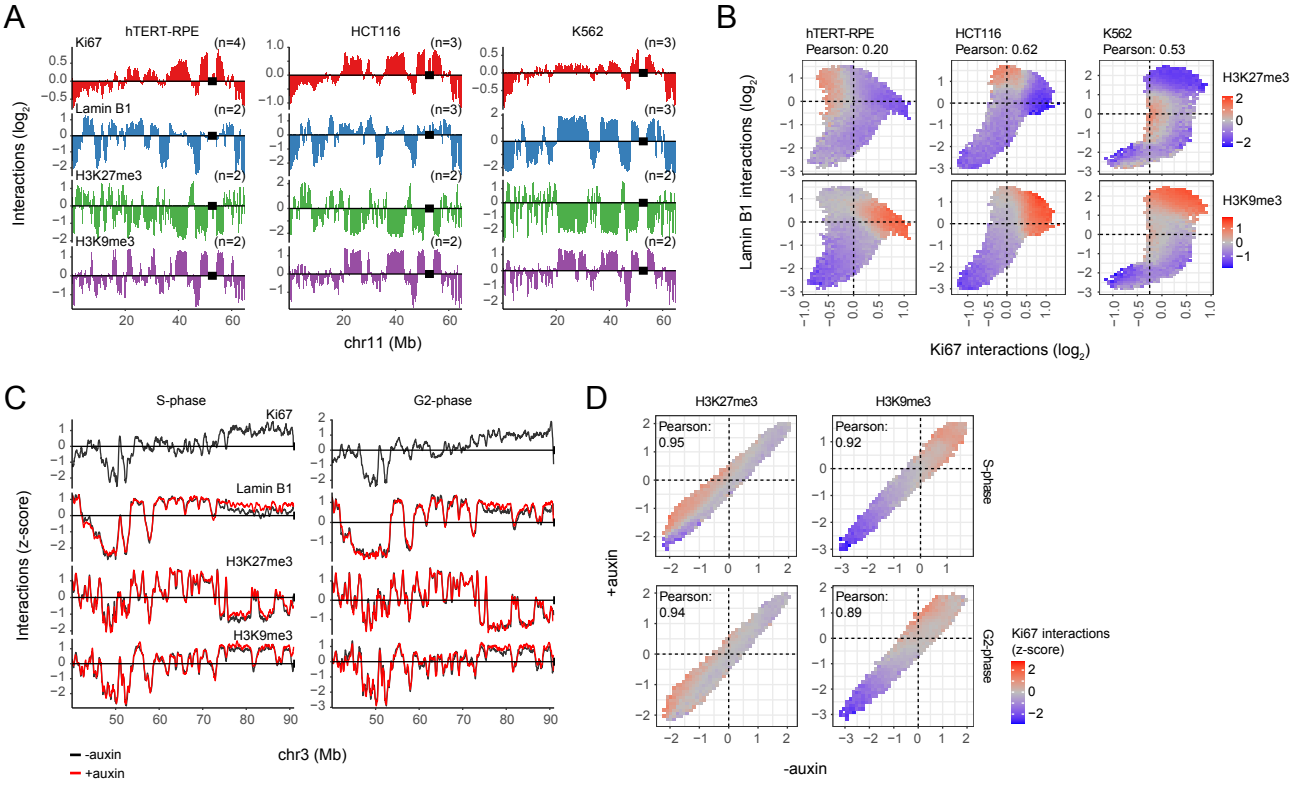

Fig 6. Comparison of the Ki67 and Lamin B1 balance with H3K27me3 and H3K9me3

(A) Comparison of Ki67 interactions with Lamin B1 interactions and H3K27me3 and H3K9me3 histone modifications for a representative genomic region. Data profiles are averages of n pA-DamID experiments and smoothed with a running mean across 9 50kb bins. Centromeres are highlighted by black bars.
(B) Binned scatterplots of Ki67 and Lamin B1 interactions as in (Fig 4B), colored according to the mean H3K27me3 and H3K9me3 signals.
(C) A similar figure as (Fig 5B), but additionally showing the effect of Ki67 depletion on H3K27me3 and H3K9me3.
(D) Similar plots as (Fig 5D), but instead showing H3K27me3 and H3K9me3 at normal and depleted Ki67 levels. Bins are colored by the Ki67 interactions in cells with normal Ki67 levels.

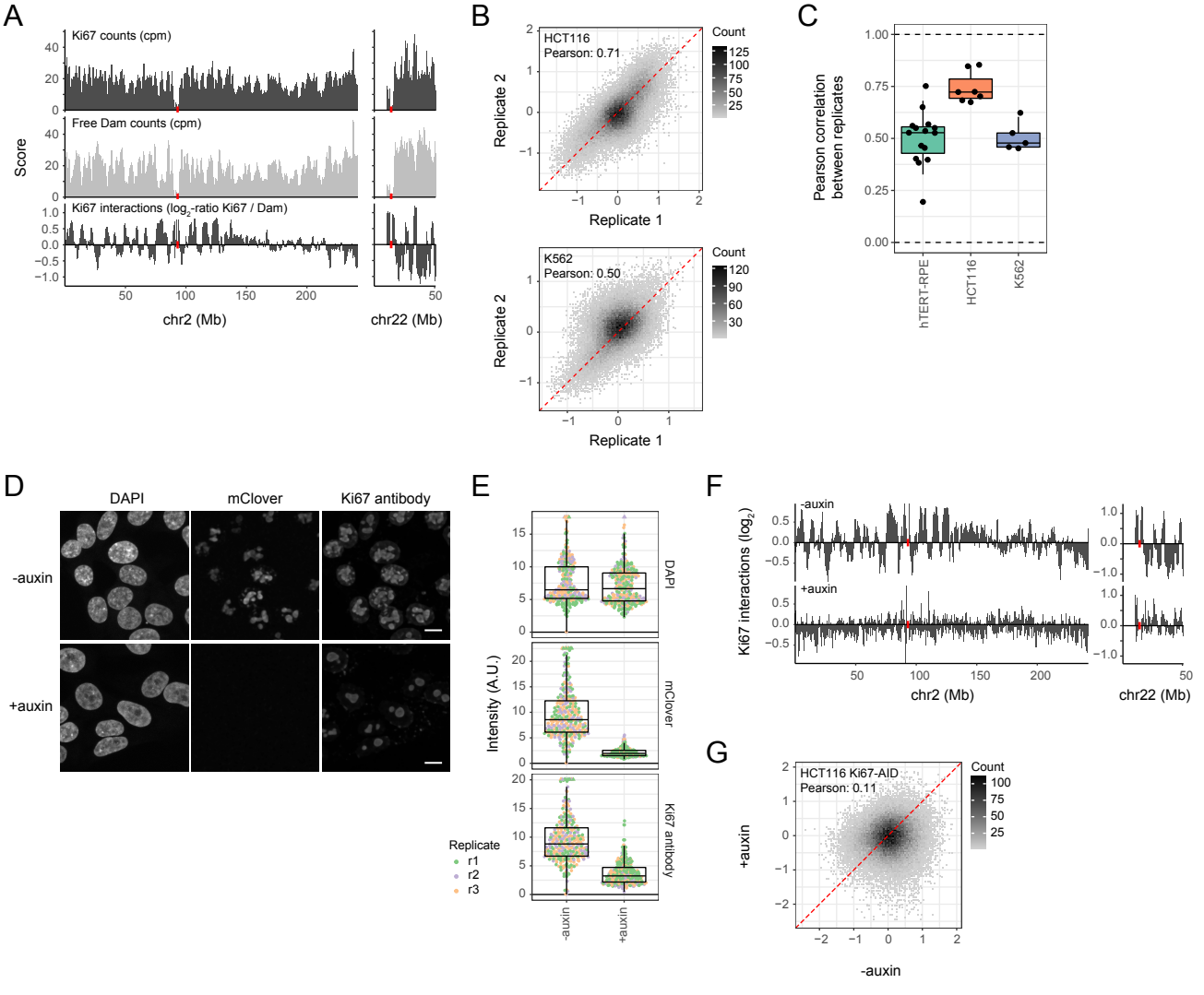

Fig S1. Additional information and controls for Ki67 pA-DamID

(A) Example of raw Ki67 pA-DamID profiles for a representative experiment in HCT116 cells. m6A-marked DNA is specifically amplified, sequenced, counted in 50 kb bins and counts-per-million normalized (cpm) for Ki67 (top profile) and free Dam (middle profile). A log2-ratio between Ki67 and Dam accounts for DNA accessibility and amplification bias, and is used as a measure of Ki67 interactions. Data profiles are smoothed with a running mean across nine 50kb bins for visualization purposes. Centromeres are highlighted by red bars.
(B) Replicate experiment correlations for Ki67 interactions (log2-ratios) measured in unsynchronized HCT116 cells (top panel) and K562 cells (bottom panel).
(C) Overview of Pearson correlations between replicate experiments for all experimental conditions studied throughout this manuscript, separated by cell line and including perturbation experiments.
(D) Representative maximum projections of confocal microscopy stacks of HCT116 Ki67-miniAID-mClover cells (HCT116 Ki67-AID in short) with normal (top panels) and auxin-mediated depleted Ki67 levels (bottom panels). Ki67 levels were visualized directly by mClover fluorescence, and indirectly by immunofluorescence with a Ki67 antibody. Scale bar: 10 µm.
(E) Quantification of Ki67 levels measured by mClover (middle panel) and immunostaining (bottom panel) from three independent replicates. Every point represents a single cell.
(F) Two representative chromosomes showing the effect of auxin-mediated Ki67 depletion in HCT116 Ki67-AID cells on Ki67 interactions as measured by pA-DamID. Data are averages of two biological replicates and smoothed with a running mean across nine 50kb bins. Centromeres are marked by red bars.
(G) Correlation of all 50 kb genomic bins from profiles described in (F).

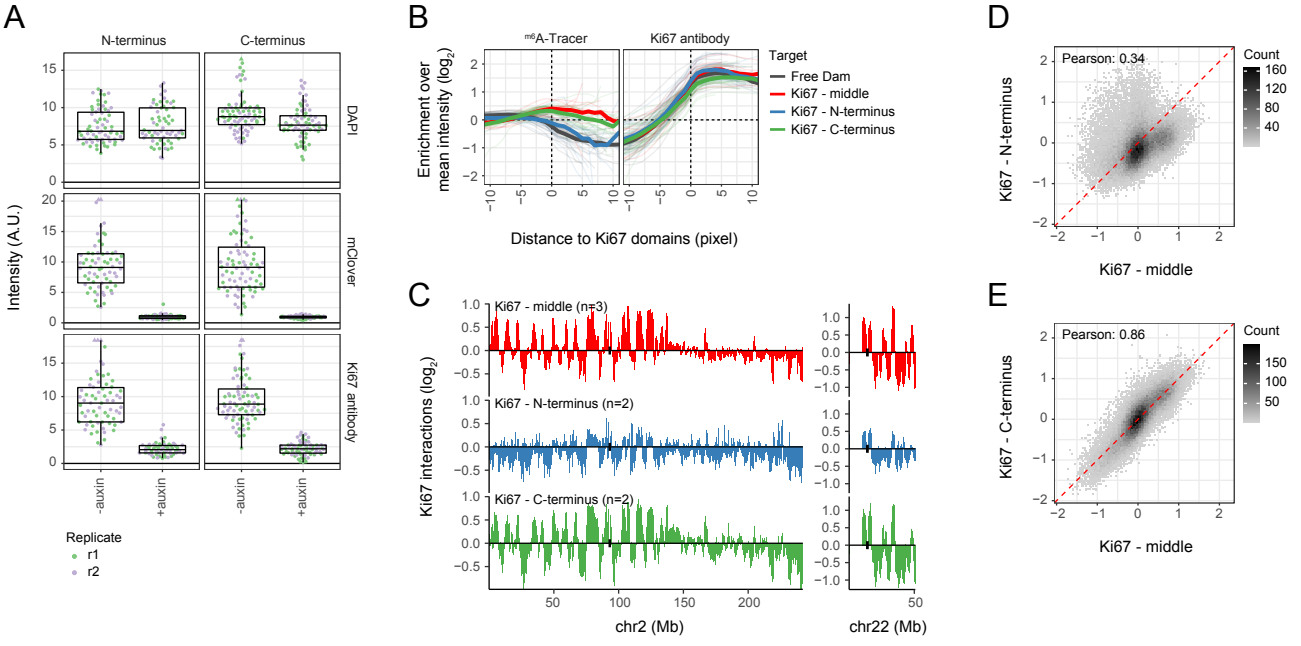

Fig S2. Ki67 interactions are reproducible between antibodies

(A) Quantification of Ki67 levels as described in (Fig S1D-E) based on mClover and Ki67 immunostaining signals in HCT116 Ki67-AID cells using different Ki67 antibodies. For this experiment, single confocal microscopy sections from the middle of cell nuclei were used rather than maximum projections from entire nuclei. Results are combined from two biological replicates.
(B) Quantification of m6A-Tracer enrichment around Ki67-marked nucleoli, as described in (Fig 1B-C). Results are combined from one (middle-targeting antibody) or two (N- and C-terminus antibodies) biological replicates. Data from Fig 1C are not included here.
(C) Ki67 interactions on two representative chromosomes as determined by pA-DamID using three different Ki67 antibodies. Data profiles are averages of n biological replicates and smoothed with a running mean across nine 50kb bins. Centromeres are highlighted by black bars.
(D-E) Correlation of all 50 kb genomic bins between Ki67 interactions profiled with the middle-targeting antibody and the N- (D) and C-terminus antibodies (E).

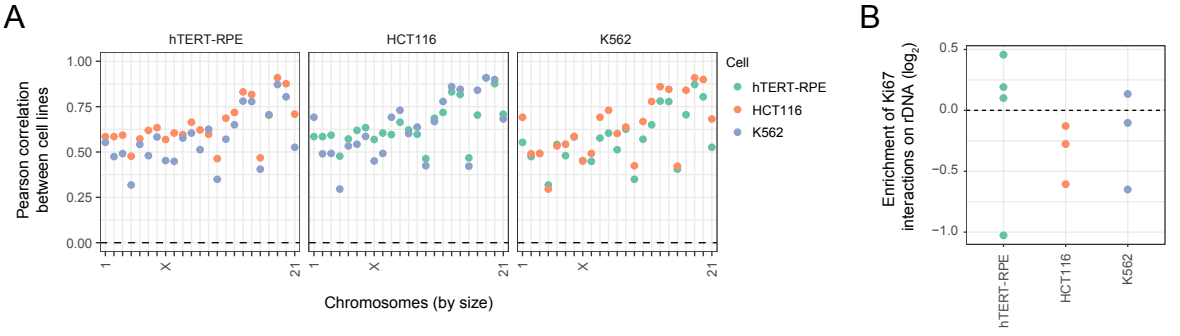

Fig S3. Ki67 interactions are more conserved on small chromosomes, and are not enriched at rDNA repeats

(A) Pearson correlations between cell lines along all 50 kb genomic bins of individual chromosomes. The panel title indicates the first cell line and the color indicates the second cell line between which the correlation was calculated.
(B) Enrichment of rDNA sequences detected by Ki67 pA-DamID compared to the Dam control.

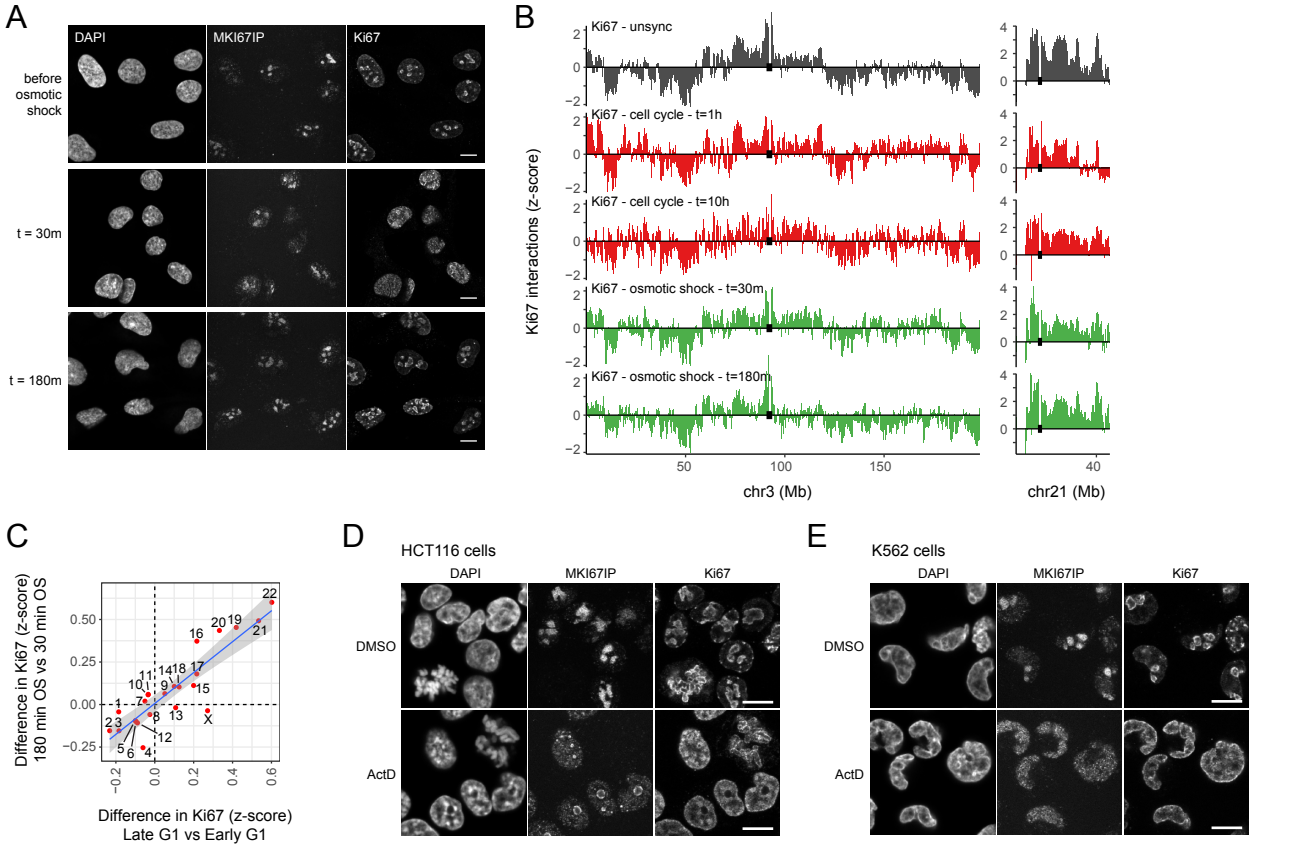

Fig S4. A short osmotic shock recapitulates Ki67 maturation from PNBs to nucleoli

(A) Representative confocal microscopy sections of hTERT-RPE cells before a 15-minute osmotic shock (0.2x PBS) (top panels), and after 30 and 180 minutes of recovery in complete medium (middle and bottom panels). Formaldehyde-fixed cells were stained for MKI67IP and Ki67. Scale bar: 10 µm.
(B) Representative chromosomes showing Ki67 interactions in unsynchronized hTERT-RPE cells, two interphase time points (data are the same as in Fig 2C) and the two time points following osmotic shock. Note that the regions that change Ki67 interactions during interphase show the same trends after the osmotic shock. Data profiles are averages of two experiments and smoothed with a running mean across nine 50 kb bins. Centromeres are highlighted by black bars.
(C) Changes in chromosomal distributions of Ki67 are similar for progression in G1 phase (x-axis: difference in mean interactions per chromosome between 10h and 1h after mitosis) and upon recovery from osmotic shock (y-axis: difference in mean interactions per chromosome between 180 min and 30 min after termination of the osmotic shock (OS)).
(D-E) Representative confocal microscopy sections showing the effect of ActD on nucleolar morphology in HCT116 (D) and K562 cells (E), as described in (Fig 3A). Scale bar: 10 µm.

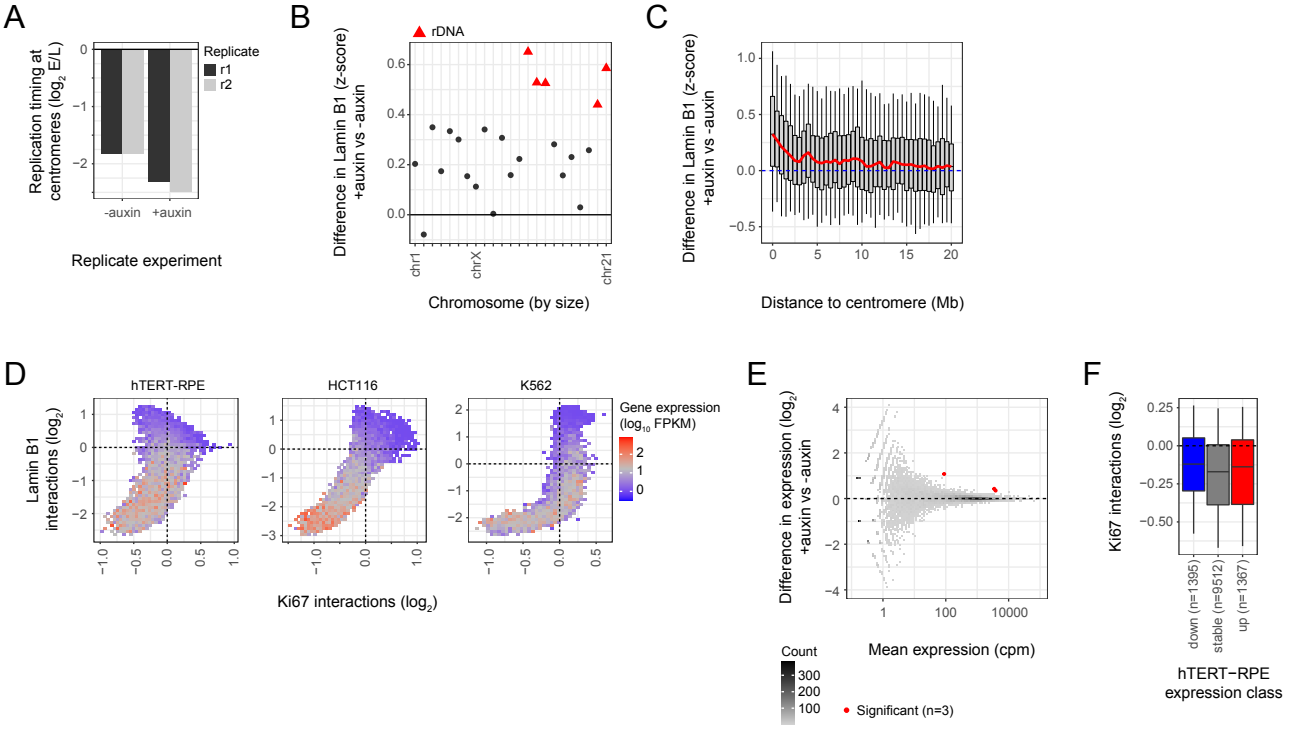

Fig S5. Loss of Ki67 interactions does not correlate with gene expression changes

(A) Bar plot showing average replication timing (log2-ratio Early/Late) for centromeres. All reads were selected that aligned to regions marked as centromeres (UCSC Table browser; hg38 centromeres) regardless of their mapping quality and, following counts-per-million normalization, the E/L ratio was calculated between the total centromeric counts. Between 3-5% of the late-fraction mapped to centromeres.
(B-C) Similar plots as (Fig 5G-H), but showing differences in Lamin B1 interactions instead.
(D) Similar plot as (Fig 4B), but instead highlighting for every gene the expression level (in log10 FPKM). Expression data are used from [30, 65-70] (see Methods).
(E) Scatterplot of mean gene expression (counts per million; cpm) versus expression difference (log2-fold change) following auxin-mediated Ki67 depletion in HCT116 Ki67-AID cells. Significant genes (Benjamini-Hochberg adjusted p-value < 0.05) are highlighted in red.
(F) Boxplots showing Ki67 interactions for differentially expressed genes following Ki67 depletion in hTERT-RPE cells. Gene expression calls are from [30]. Boxplots: horizontal lines represent 25th, 50th, and 75th percentiles; whiskers extend to 5th and 95th percentiles.